Design, Development and Force estimation of a Tendon-driven Steerable Catheter based on Image-processing and Learning Approaches

Pegah Yaftian

A Thesis

in

The Department

of

Mechanical and Industrial Engineering

Presented in Partial Fulfillment of the Requirements

for the Degree of

Master of Applied Science (Mechanical Engineering) at

Concordia University

Montréal, Québec, Canada

December 2021

CONCORDIA UNIVERSITY

School of Graduate Studies

This is to certify that the thesis prepared

By: **Pegah Yaftian**

Entitled: **Design, Development and Force estimation of a Tendon-driven Steerable Catheter based on Image-processing and Learning Approaches**

and submitted in partial fulfillment of the requirements for the degree of

Master of Applied Science (Mechanical Engineering)

complies with the regulations of this University and meets the accepted standards with respect to originality and quality.

Signed by the Final Examining Committee:

_____ Chair
Dr. Name of the Chair

_____ External Examiner
Dr. Dr. Arash Mohammadi

_____ Examiner
Dr. Dr. Mojtaba Kheiri

_____ Supervisor
Dr. Javad Dargahi

Approved by _____
Martin D. Pugh, Chair
Department of Mechanical and Industrial Engineering

_____ 2021

_____
Amir Asif, Dean
Faculty of Engineering and Computer Science

Abstract

Design, Development and Force estimation of a Tendon-driven Steerable Catheter based on Image-processing and Learning Approaches

Pegah Yaftian

In this research, an image-based force estimation schema for tendon-driven steerable catheters with the application in robot-assisted tissue ablation procedures was proposed and validated. To this end, initially, an inverse kinematics solution for modeling the catheter deformation and alternatively estimating the contact force between the catheter and cardiac tissue was proposed. Next, an in-house tendon-driven radio-frequency ablation catheter was designed and developed. Afterwards, the developed robotic catheter intervention system was equipped with a software-hardware-integrated robotic system for controlling and recording the deformation of the catheter and other motor stimuli. Furthermore, the performance of the developed model in contact force estimation was improved by various learning approaches. Validation studies were performed on phantom tissue as well as excised porcine tissue. The results of the validation studies showed that the proposed image-based inverse kinematics solution model have the maximum root-mean-square error was 0.01, 0.009, and 0.012 N for the tests on the porcine atrial tissue. Furthermore, adopting a machine learning pipeline stacked to the previously validated model exhibited an accuracy of 97.0%, 97.7%, 97.6%, and 97% and 97.9%, 98.3%, 97.8%, and 98.8% for the Support vector machine, Random Forest, AdaBoost, and Deep Neural Network, respectively (for three different movement manner). For yielding optimal models, hyper-parameter search were performed for all proposed learning models. In summary, the proposed force estimation system did not necessitate the utilization of force sensors and could successfully contribute in operation rooms during cardiac manipulation for providing force feedback to novices and expert surgeons.

Acknowledgments

First and foremost, I would like to acknowledge my family love and endeavours. Mohammad Reza, my father, who has been my biggest role model and a great source of inspiration since I was born. My mother, Leila, whose devotion, strength and sacrifices have been always empowered me to come through the hurdles. Pouya, my younger brother, with whom I shared all my childhood memories, who will always have a piece of my heart with him.

Next, I would like to thank my mentor, Dr. Naghmeh M.Bandari for her constant help, dedicated support and wise guidance throughout this research project. I can not be thankful enough for her assistance throughout the research whenever was needed.

I would also like to express my deepest gratitude to Dr. Amir Hooshiar for his insightful comments during my project.

I would like to be thankful for my colleagues and friends; specifically, Amir, Hamidreza, Hamidreza and Majid.

Lastly, I am blessed for having beloved people around me; whose love always warms my heart, despite miles of distance. I would like to express my love to my friends: Elahe, Kiana, Sheila, Parisa, Naghmeh and Lucia.

Contents

List of Figures

List of Tables

To:

My Beloved Family

In Memory of:

Passengers in the flight752,

esp. My Friends

Nasim RahmaniFar

&

Amirhossein Saeidinia

Chapter 1

Introduction

1.1 Background

1.1.1 Cardiac arrhythmia

Cardiovascular diseases (CVDs) have become predominant cause of death globally, with over 17.3 million deaths per year. By the year 2030, it is estimated that the CVD mortal rate reaches 23.6 million deaths which make up more than 30% of the worldwide moralities [2]. CVD could catastrophically result in cardiac structural distortion associated with false electrical signals and cardiac arrhythmia [3]. Arrhythmia may occur at any age and is characterised by a heartbeat that is either too slow ($<$ 60 beats per min) or too fast ($>$ 100 beats per min). Moreover, arrhythmia is the second most common CVD, i.e., uncoordinated contraction and relaxation of myocardium, and can lead to blood clot, stroke and hear failure [4–6]. Fig.1.1 depicts the electrical conduction system of the heart and an Electrocardiogram (ECG) of a normal heartbeat.

Atrial Fibrillation (AF) one of the most common arrhythmia in elderly people is a condition in which the heart's electrical signals are violated in pulmonary veins(PVs), this causes chaotic rhythm in atria and hence, it won't be able to contract and effectively direct the blood to the ventricle. According to American Heart Association (AHA) statistics, AF prevalence is forecasted to increase from 5.2 million in 2010 to 12.1 million cases in 2030 [7].

As shown in Fig. **??**, ECG gives a detailed understanding of the patient cardiac health condition.

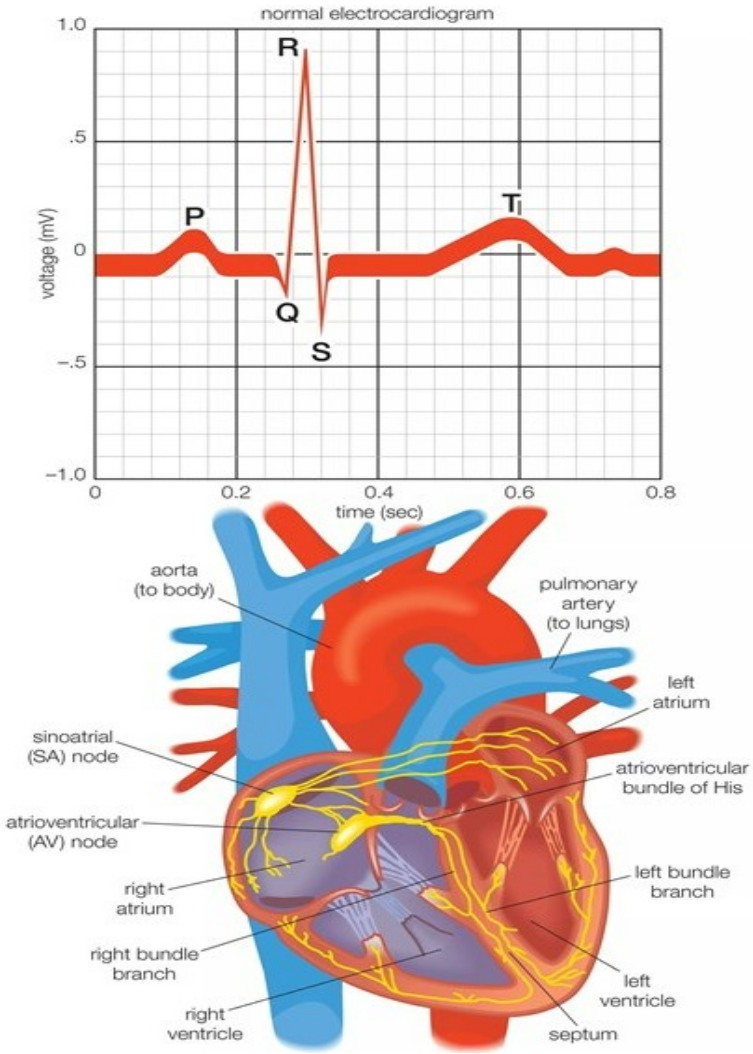

Figure 1.1: Heart function [9]

For People who suffers from cardiac arrhythmia,the ECG depicts either no pattern of frequency or eliminating P wave. Hence, in AF, the upper chamber of the heat (atria) quivers and beats in-coordinately with the ventricles [8] (Fig. 1.2).

1.1.2 Treatment

The current treatment options for AF is listed below [11]:

- pace makers and defibrillators
- Catheter-based ablation

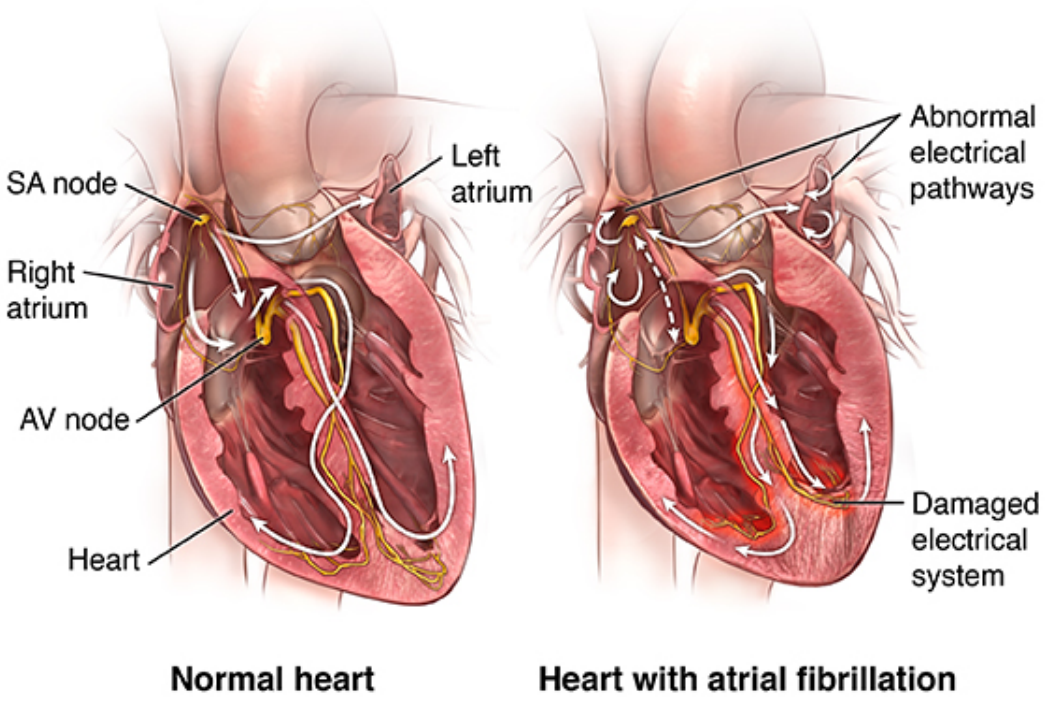

Figure 1.2: Atrial Fibrillation [10]

- Antiarrytmatic drugs (AAD)

while the complications of implementing permanent pace makers and high recurrence rate and inapplicability of AADs in severe ventricular arrhythmia cases has limited the use of these treatments, catheter-based ablation is a promising treatment of choice with a success rate of 97% [11, 12]. During ablation procedure, the inserted catheter ablates the abnormal cells to block distributed signals and restores normal heart function [13]. There are two energy source for catheter- based ablation including: radio-frequency (RF) and cryothermal energy [14].The radio-frequency ablation(RFA) has been considered to be the standard treatment and is opted more frequently than cryoablation [13, 15]. Despite the clinical success of the RFA, the outcomes of the procedure is highly depended on durable lesion formation(burnt area) within the atrial wall [16]. Creating a durable RF lesion is influenced by RF current delivered to the tissue, the period of RF energy delivery and the amount of catheter-tissue contact force; hence, achieving a desired contact force is of prime priority [17, 18].

During RF, a thin and hollow wire (catheter) is percutaneously inserted into the femoral veins and

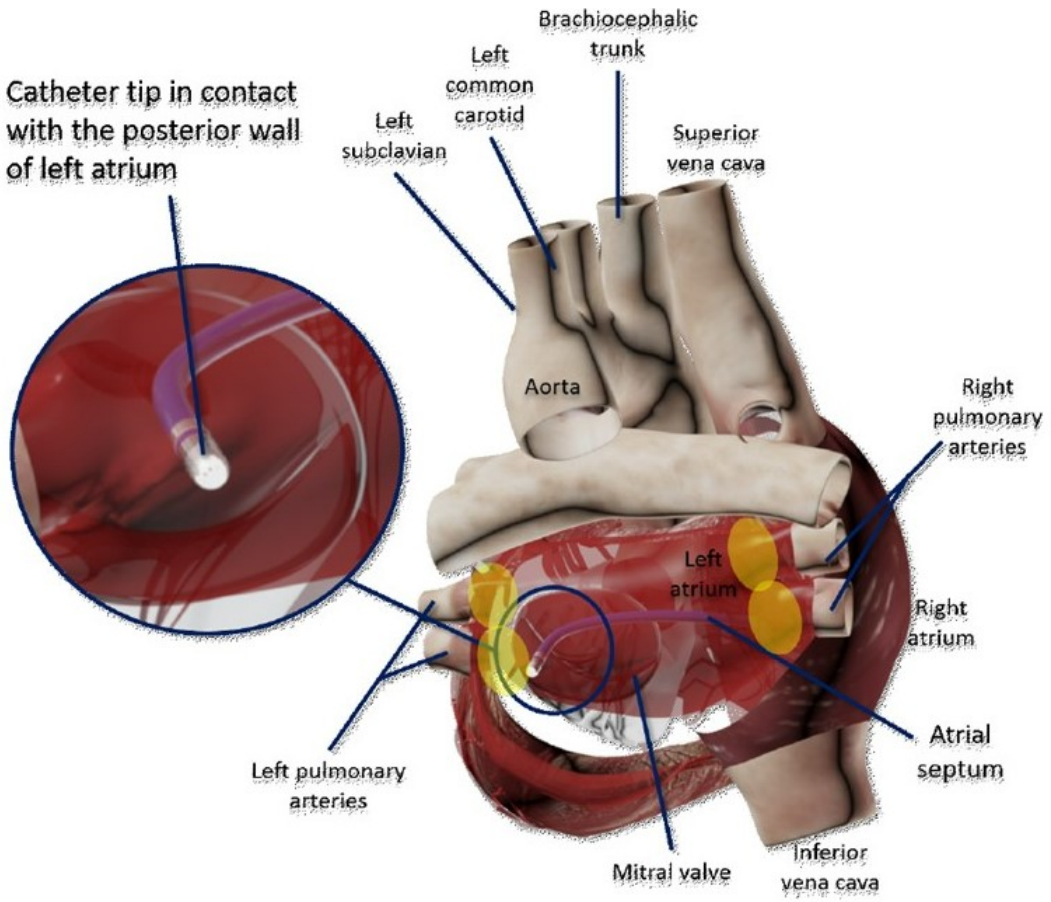

Figure 1.3: To access the ablation target areas (yellow), RFA catheter is passed through the atrial septum, i.e. wall separating left and right atria. Catheter steerability plays a crucial role in both reaching the target areas and maintaining the contact during the ablation procedure [1].

oriented within the heart chambers. Once the catheter tip (typically 7 French in size with a tip electrode size of 4 mm) came in-contact with the site of origin of the arrhythmia, a lesion with 2 mm depth is created. [19, 20]. Steerable catheters tip- embedded electrical electrodes facilitated the accurate delivery of RF energy to the target regions. Such catheters are widely adopted in cardiology, neurology, and endovascular minimally invasive surgery, diagnosis, and treatment [21]. Fig.1.3 depicts the configuration of a steerable catheter during RFA procedure inside the heart chamber.

1.1.3 State-of-the-art for treatment

Historically, cardiovascular diseases (CVDs) have been treated using open-surgery techniques. However, by emergence of intervention radiology in 1960, minimally invasive surgery is currently

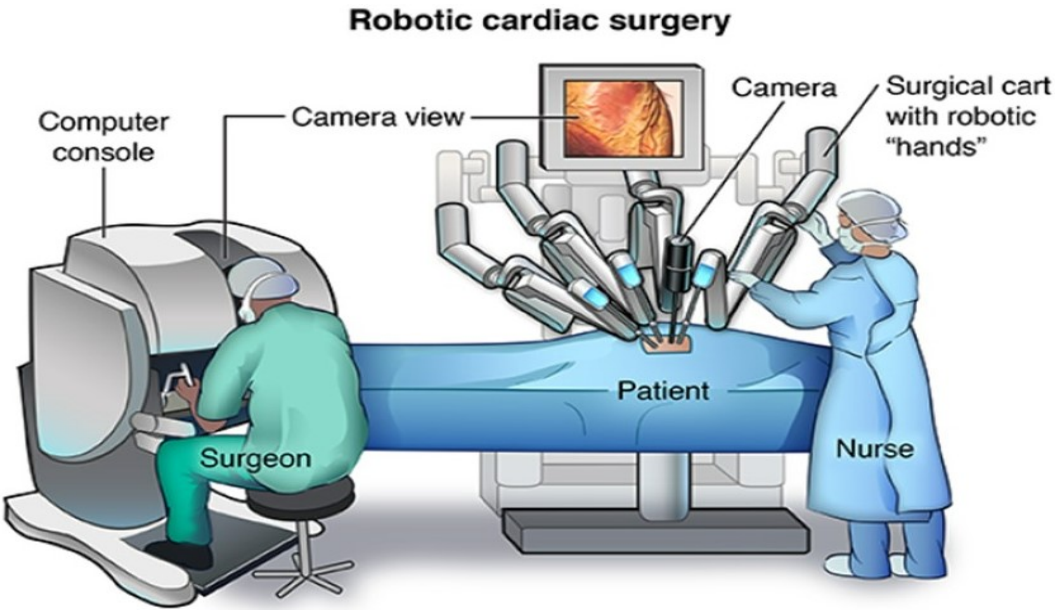

Figure 1.4: A schematic positioning during a robot-assisted cardiac surgery is shown, heart surgery is being done through very small cuts in the chest. The surgeons are doing the manipulations using tiny instruments and robot-controlled tools to do heart surgery [22].

a commonplace and continuing its development. For diagnose and treatment of cardiac electrophisological diseases, catheters were developed. Since mid-2000s by developing a number of commercial robotic systems, robot-assisted catheterization have been the current state-of-the-art technology to perform cardiac interventions and alleviate the shortcomings of conventional interventions [23,24]. Robotic- assisted cardiovascular intervention are mostly deployed in percutaneous coronary intervention (PCI), percutaneous peripheral intervention (PPI), electrophysiological intervention (EPI) [24]. A schematic robotic-assisted surgery is depicted in Fig. 1.4.

1.1.4 Limitations of the state-of-the-art

Robot-assisted catheter interventions (RCIs) as a subset of robot-assisted minimally invasive surgery (RMIS), promise improved precision and stability in catheter navigation, enhanced operator comfort, dexterity, visualization, and reduced radiation exposure. Despite the advantages of RCI systems, some studies escalate serious doubt about its efficiency as the commercially available systems do not provide haptic, force, and tactile feedback to the operator [23, 25–27]. These constraints are considered as the predominant factors avoiding RCI technology to be widely expanded

in minimally- invasive surgery (MIS).

During manual catheterization, the operator navigates the catheter through manipulating the proximal handle outside the patient's body, hence he/she can relies on haptic cues result from sensing trivial forces/torques at the fingerprint. However, in the case of RCI systems, the tool-tissue force feedback is required to be compensated [28]. Moreover, the steep learning curves for training novices associated with endovascular catheterization is considered as another limitation. The training of endovascular skills has relied on various modalities including synthetic models, animals, cadavers, and virtual reality (VR) simulators [28, 29].Despite this conflict of opinion, a recent study reported that using RCI systems has been increasing in number and variation of procedures [30].Nevertheless, the common ground between the critical and complementary opinion is the recognition of the force feedback loss [30, 31].

According to literature, the efficiency of RFA procedure is highly dependent on maintaining contact force in the rang of $0.2 \pm 0.1N$ between catheter tip and atrial wall [32–34]. Applying a contact force below the desired range will lead to an unsuccessful treatment, on the other hand, preserving a force contact exceeding 0.3 N can cause catheter over-steering, vessel rapture and atrial puncture [35, 36].

Teleoperation has so far been equipped with haptic feedback using two main approaches: sensor-based a.k.a *direct* feedback; and model-based a.k.a *sensorless* feedback. In the sensor-based approach, the force feedbacks (force cues) are realized through installing a sensor or array sensors at the catheter tip [37–39]. In sensor-based approach several factors are need to be considered in designing a force sensor including: sensor thickness, flexibility, magneto-electric effect and mass-fabrication capabilities [40, 41]. On the other hand, the model- based approach utilized computational estimation of the force based on mechanistic or heuristic models to predict the contact force [42].The computational models mostly consist of mechanical model of the catheter, image analysis technique, force estimation module and learning algorithms [24].

1.2 Problem definition

Robot-assisted cardiovascular intervention (RCI) potentials for providing an accurate and safe dynamics for both surgeon and patient have been vividly validated. However, clinical studies have declared that the prime technical limitation has been the loss of interoperative force estimation for surgeons. According to studies [28], the most considerable haptic feedback interoperatively is the insertion force noticed by surgeons.

A steerable catheter shall be flexible enough to be adopted through the complicated and tortuous cardiovascular structure. Also, the catheter control algorithm shall be precise enough to navigate the catheter toward the target location and perceive the tip-tissue contact force during ablation in the effective range. Hence, a method to measure and estimate the force at a catheter tip is an unmet clinical need.

1.3 Objectives

To overcome the gap of interoperative force estimation and control for RFA catheters, a force estimation schema based on curvature deformation of catheter inside the heart chamber (image processing), motor stimuli incorporated with learning techniques was investigated. More specifically, the following objectives were defined and followed:

(1) to propose and validate a planar mechanical model of the catheter with an unknown tip-tissue contact force

(2) to propose and validate an inverse-kinematic solution for solving catheter real-time contact force estimation through utilizing an image- based method

(3) to propose a new learning- based force estimation framework for steerable catheters

(4) to develop, implement, and validate force estimation methods through the mechanistic model combined with learning approaches which are:

   (a) image- based and compatible with 2D fluoroscopy images available at catheterization labs,

(b) independent of *a-priori* knowledge of the patient's anatomy,

(c) accurate with less than 10% error within the desired range of catheter tip.

1.4 Literature review

1.4.1 Steerable Catheters: Taxonomy

Continuum robots have been widely adopted in medical field due to their unique privileges such as high flexibility, high dexterity, promising safety, miniaturization capability and ability to work in limited and constrained environments, e.g. close human-robot interactions [43–46]. Catheter and catheter-like manipulators, as fine examples of continuum robot structures, are currently receiving high attention due to rising research interest in MIS and natural orifice translumenal endoscopic surgery [45,47].Transcatehter- based procedures have been a standard of care in cardiology by emergence of percutaneous coronary intervention for diagnosis and treatment applications [48]. With current advancements, catheters are capable of performing numerous operations including coronary stenting, repair of congenital heart defects, heart valve repair or replacement, and ablation of atrial fibrillation (AF) or ventricular tachycardia [48–50].

A catheter is a long, thin, hollow and flexible tube that is inserted through small incisions to the body cavities and allow for drainage, administration of fluids and access the targeted diagnosis/treatment spot by surgical devices [51]. A typical cardiovascular catheter is shown in Fig.1.5. One of the main challenges in catheter- based interventional cardiology and electrophysiology is to precisely position and navigate the catheter tip inside the heart chamber. This limitation is mainly a result of heart motion during heart beat and respiration. Other factors including tortuous vessel structure, complex anatomy of cardiovascular system, and and the lack of heart wall support further limit the possibility of accurate steering [53]. To overcome the catheter navigation problem, steerable catheters were emerged during past decades [54, 55]. Steerable catheters have been proven to have improvements in procedural time and safety compared to conventional catheters [23, 55]. Steerable catheters also offer out-weighted safety and effectiveness due to higher contact force control [56, 57]. A variaty of actuations methods for soft continuum robots have been proposed to enhance the capability of steering and positioning in cardiac applications, safety, and miniaturization. Depending on the actuation

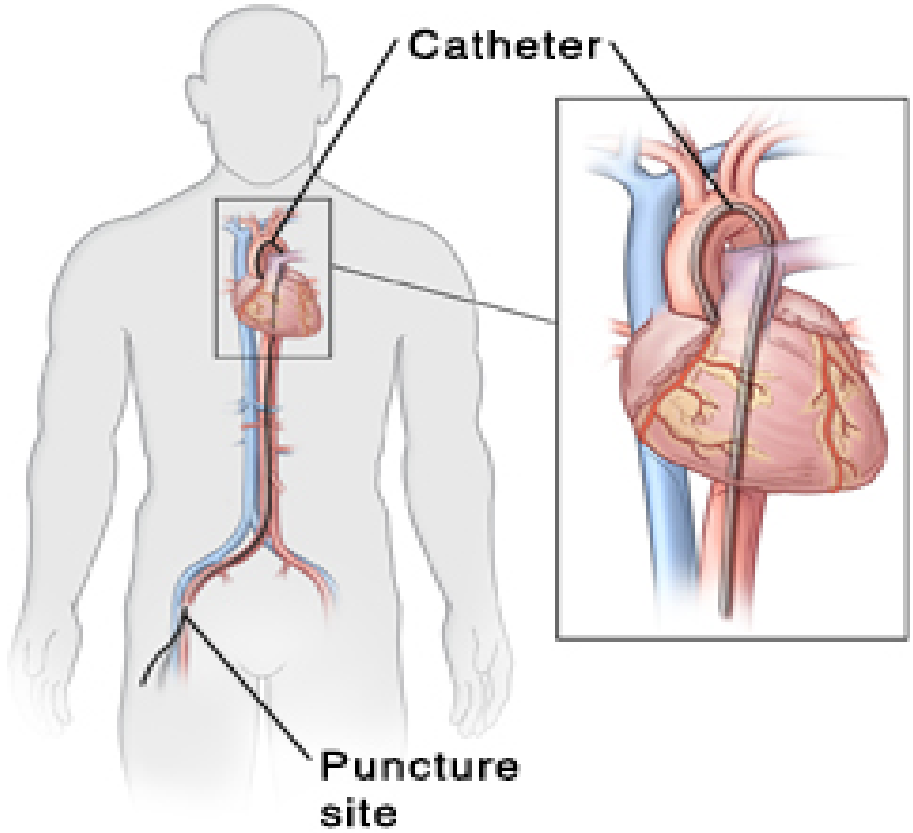

Figure 1.5: A cardiovascular flexible catheter providing a path for fluids and the surgical devices to go through it and reach the under surgery part of the heart [52].

system, steerable catheters are generally divided into two main categories: (1) force generation in the tip which includes subcategories: 1)electric actuation,2)thermal actuation,or3)magnetic actuation, (2) force transmission to the tip which comprises of 4)hydraulic chamber or 5)mechanic cable, actuation modes. Awaz *et al.* have been suggested a structured review a structured classification of steerable catheters, their actuation mode and methods used in medical applications [53].

1.4.2 Steerable Catheters: Driving Modalities

Tendon-driven steerable catheters

Tendon-driven mechanism allows for easy miniaturization in soft continuum manipulators from

medical applications to aerospace industry; hence, it is contemplated as a favorable choice in controlling the continuum robots [58, 59]. Currently, the largest and most commercially available technology for catheters is based on cable or tendon actuated steering. For instance, ”Tendril” as first catheter- like continuum robot of its kind, was developed by NASA which was intended for in-space inspection applications. The actuation method was based on sets of antagonistic tendons which were run through the entire length of robot body, and terminated at pulleys inside the manipulator structure [60]. Fig. 1.6 depicts the steerable tendon- driven catheter used in used in *Sensei X*®. The catheter is navigated remotely through a system of pulleys which allows for a large maneuverable space inside the atria [61]. For determining the force at the catheter tip several models have been suggested.Ganji *et al.* [62] and Camarillo *et al.* [63] have postulated mechanical models based on multi-body dynamics for estimating the contact force at the tip of the a tendon- driven catheters. . In this model, a single section of the manipulator is considered as a cantilever beam which demonstrates large deformation as a result of tendon actuation.

Another principal feature in designing tendon- based soft robots is the backbone design.Researchers [64] describes and discusses the history and state of the art of continuous backbone soft robot manipulators.In this review, design of continuum robots have been categorized in 5 groups including: concentric tube designs, locally actuated backbone design, variable backbone stiffness. In tendon-driven robots, tension forces at the base of tendons, produce torques at the distal points, and cause bending. One widely- adopted choice for the core backbone element is a compressible mechanical spring. In an early effort, Hirose *et al.* [66] produced a mechanical spring- based design of continuum robots. Using compressible spring may lead to bending control complexities; hence, a flexible incompressible rod could be an alliterative for the backbone element [67]. This course has been successfully implemented in various soft robots [68–70]; however incorporation of backbone extension is a shortcoming of this approach. Moreover, spring based designs can easily retrieve its original shape, at the resting point, and navigate with smaller tendon tensions. For accurately guide tendon- driven catheters and control force at the target position, slack [71] and backlash [72] are need to be prevented. In this respect, most implementations simultaneously actuate all tendons [73] or sets of agonist- antagonist tendons with a single actuator [74], with a spring mechanism to compensate the backlash and slack. A compressible spring-based tendon-driven backbone soft robot

Figure 1.6: Steerable tendon-driven catheter used in *Sensei X*® [65]

was developed for sinus-surgical [75], ACL-surgical [76], and laryngeal- surgical applications [77]. Having mentioned undeniable advantages of tendon-driven catheters, there are drawbacks such as nonlinear friction, hysteresis, sterilization difficulty, fatigue, force transmission hurdles and control problems [78, 79].

Pneumatic-driven steerable catheters

Pneumatic(hydraulic)- driven soft robots made up of chambers from fibre- reinforced stretchable rubbers. The pressure inside the chambers is controlled by flexible tunes connected to electro-hydraulic valve. the tubes are being pressurized by fluid and gas during cardiovascular and bronchial surgery, respectively. As the pressure inside the tubes increases, the flexible tip of the catheter deforms in a direction opposing the position of pressurized tube [80]. Locating a flexible and in-extnensible strain limiting layer at the base of soft robots with pneumatic actuation, is a key factor to generate a bending motion [81, 82]. In an effort Miles *et al.* [83] designed a pneumatic- driven

catheter in which tubes are located on both sides of catheter and reached to an elastomeric catheter tip; the tip was equipped with some steering lumens which are offset from the catheter . In such catheter designs, the bending behaviour is controlled through a pneumatic or hydraulic pressure source or by heating a thermally expandable material filling the lumens [83].Francois *et al.* also designed a hydraulically-driven catheter utilizing three elastic nickel bellows and selected physiological to increase the catheter safety [84]. In another effort [85], a Ti–Ni super-elastic alloy tube was hollowed out and covered with a silicon rubber to fabricate a pneumatic catheter having one degree of freedom. Currently, the MEMS techniques are employed in developing the miniaturized pneumatic- driven catheters [86].

The shortcoming in use of hydraulic- driven soft robots is the complexity in modeling and controlling arises from deformation exhibited by the nonlinear elastomer materials [87].To address this challenge several solutions have been proposed including experimental characterization of bending geometry [88] and FEA analysis [89].

The primary difference of typical pneumatic actuators (such as the McKibben-type actuators) to pneumatic soft robots is that the latter group are developed entirely using soft elastomers. Thus, soft pneumatic actuator are a desire alternative for certain applications; but unknown characteristic of them due to softness and customizability has been necessitated strict functional requirement [90]. In an effort [91], a soft penumatic- driven actuators were designed with a combination of elastomeric (hyperelastic silicones) and inextensible materials (fabrics and fibers). The proposed fiber-reinforced bending actuators compared to existing soft pneumatic- driven actuators [90,92,93] have a much simpler tubular geometry that offers ease of manufacture, and allows for nontrivial deformations.

Having all being said, pneumatic- driven catheters is not considered a desirable option to be used in RFA applications. The high risk of air/fluid leakage throughout the cardiovascular structure may lead to mortal complications. Moreover, the hydraulic resistance is inversely proportional to the square of catheter diameter, hence the customary RFA catheter diameter with 18 Fr of length mandates high pressure for deformation; consequently, the risk of leakage and bursting escalates. The bulky design of pneumatic- driven catheter modality is another shortcomings prevent the efficient use of them in cardiovascular applications.

Magnetic-driven steerable catheters

In the magnetic modality navigation, a catheter with a magnetic tip is steered throughout the vasculature. The magnetic field is provided by the means of large magnets places on the patient's sides [21]. The commercially available products for magnetic navigation catheters include Niobe® ES magnetic navigation system (Stereotaxis, St. Louis, MO, USA) (Stereotaxis 2016) and Catheter Guidance, Control and Imaging-Maxwell (CGCI) (Magnetecs, Inglewood, CA, USA) (Magnetecs 2016). The magnetic field can also be a result of the electromagnets [94–96].For instance, Stereotaxia Inc. introduced a magnetic navigation system called Telstar [95] operate based on three orthogonal electromagnets. In another studies, the feasibility of a magnetic-assisted navigation system during percutaneous coronary intervention (PCI) [97] and pulmonary vein ablation (CPVA),was evaluated [98]. Even though the results proved the magnetic- driven modality to be a safe treatment option with a short learning curve method, however the compatibility of magnetic field with medical devices e.g. MRI and electrical activity of the heart have not been investigated.

Smart material-driven steerable catheters

Shape memory materials (SMMs) are capable of retaining a predetermined geometrical shape with heating following a plastic deformation. Based on mechanical properties of SMMs, they are not only applicable in traditional endoscopic or surgical procedures but also for catheter- like procedures that require miniaturization. For instance, shape memory alloys (SMAs) have been widely adopted due to their biocompatibility, corrosion resistance, non- magnetic behaviour, high energy density to apply concentric contact force and fabricability in various shapes and dimensions.Accordingly, SMM-driven catheter systems are proposed to address drawbacks of cable- driven approaches [99]. Thermally active materials actuated by an electrical current can be stimulated using two main thermal actuation: 1) isolated thermal actuation, and 2) integrated thermal actuation [53]. The isolated thermal actuation relies on the application of an electric current to isolated thermal elements (SMAs). SMAs positioned inside or on the catheter tip and isolated from the rest of catheter body.A number of different element types are available in the structure including: SMA wires, micro-coils, and plate actuators. As an example , a prototyped catheter [100] having three straight stainless steel tip segments connected to each other by SMA wire actuators, was developed. The developed SMA-based catheter was intended to be used as a steerable delivery tube for percutaneous needle- based

diagnostic applications, e.g. prostate and breast biopsy. The latter group which is integrated thermal actuators provide both the catheter actuation and catheter tip. Due to less interconectivity and structure complexity of the integrated thermal actuators compared to isolated thermal actuation, it has certain advantages. In addition, it equipped catheter with a proper axial stiffness and less energy loss in its bending mechanism [53]. In an effort Langelaar and van Keulen [101] presented a SMA thermal actuator in the form of a laser-machined SMA tube. NiTi alloy were used to fabricate the structure and actuation of the tube. local change in SMA bending behaviour was opt through generating heat by applying voltage in electrodes embedded in the catheter structure.

For measuring the contact force in SMA- driven catheters piezoresistive and strain- gauge sensors were employed [102,103]. The mentioned sensors are at high risk to have undesirable interfere with electrical devices; additionally, the accuracy of the sensors can hugely be affected by electrolytic nature of blood flows around the sensor locations in the body [104]. The challenges arise from optical sensor- embedded surgical tools is widely elaborated [40,41].Therefore, the SMA- based navigation system is yet to be fully adopted in cardiovascular systems [105]. Noteworthy, the SMAs exhibit several limitations including low strain, limited speed (low bandwidth which significantly relies on mechanothermal characteristics) and providing high current to fulfill sufficient activation temperature [79].

Comparison of driving modalities

Steering performance is the preliminary factor in evaluating the various driving modalities in remote catheters. A desired drive system should steer and navigate catheter accurately to the target position and maintain the sufficient tip-tissue contact force. Increasing the degree of freedom (DOF) of catheters will expand the working environment of the device. Different components are adopted in various driven modalities are adopted to expand the working environment of systems; e.g. in tendon- driven actuation, increasing the number of tendons will result in number of DOF expansion. As the number of DOF, the system gets more complex. As a result, in tendon- driven catheters higher DOF leads to friction, buckling and cable wedging.

On the other hand,SMMs are not practically considered super- elastic materials and analysing their partially plastic effect demands meticulous analysis such as finit-element modeling (FEM). In pneumatic and hydraulic actuators, precision and force control can possibly cause problem since slight

differences in gas compressibility, flow characteristic at the entrance valve, and friction can easily cause nonlinearities. Furthermore,parameters of these systems are affected by temperature, shape and friction [106]. Having all being said, Tendon- driven modality has been proved to be a desirable choice to be used as actuation systems in RFA RCI catheters.Tendon- driven catheters comparatively offers less complexity, cost- effective and more applicable solutions.

1.4.3 Steerable Catheters: Modeling as Soft Robots

As depicted in Fig. 1.7, in model- based force estimation system a computational approach is used via adoption of boundary conditions from sensors, live imaging, and a mechanical model of the catheter. Due to the high risk of inaccuracy of force feedback during remote cathterization; the solution model is required to be precise, real- time and stable [105, 107]. As a result of high ratio of length to diameter of the catheter, the are frequently modeled as a one-dimensional beam-like structures, from the kinematic point of view, 4 main approaches have been opted: continuum mechanics-, multibody dynamics-, differential geometry-, and particle-based models.

Continuum Mechanics Models

Continuum models are categorized as model-based haptic feedback [24], in which the force is estimated through computation, live imaging, boundary conditions of sensors and mechanical model of the catheter. In an early study [109], a continuous modeling for catheter deflection in cardiac intervention was proposed. In another effort Camarillo *et al.* [58] proposed a continuum explanation for predicting the deformation of the tendon-driven catheter in quasi-static manipulation. Though, the mentioned models required detailed information, e.g. tool-tissue contact force at the tip of the catheter and non-linear material compliance. Furthermore, both models were not applicable for real-time applications [110].Khoshnam *et al.* [111] utilized Euler- Bernoulli assumption for modeling the large deflection of a conventional steerable catheter. Due to high slenderness of the catheters, the author neglect the shear effects and out-of-plane warping of the catheter cross-section. As extension of the study mentioned above, In [112, 113], large deflection analysis method was employed to estimate the contact force at the tip of the catheter; however the error reported to be relatively high.

In another effort [114], a linear finite element model combined with Euler- Bernoulli theory yo estimate the tool- tissue contact forces between a cardiac catheter and the vessels in a vascular phantom. Nonetheless, the results shown an underestimation in comparison with clinical studies.Despite the high precision of finite element analysis (FEA) method, it can be a source of erroneous results in the absence of precise constraint definition and treatment; esp. in the case of contact force estimation [111]. Jones *et al.* [115] proposed a kinematic method for multisecion continuum robots. The kinematic method allows for real-time deflection control through mapping inputs, e.g. tendon lengths or hydraulic pressures with robot configuration.

Multi-body dynamics models

Owning the simplicity and computational efficiency of multi-body dynamics framework in modeling catheters and guidwires, it has been widely adopted in literature [24]. In multi-body systems, to derive the kinematics, the structure is approximated as a set of rigid links connected by flexible joints. Due to discrete segmentation of robot in multi-body dynamics method, it is a desirable approach to be used in robot control applications. A comprehensive review of flexible multi-body dynamics was presented in [116]. The multi- body dynamics is considered as a field which combines rigid body dynamics, continuum mechanics, finite element method, numerical, and tonsorial analysis. In an early study, Alderliesten [117] *et al.*, suggested a two- dimensional multibody system for a typical catheter. The experiment was done under assumption of constant and relatively slow speed (quasi-static) maneuver of the catheter. Ganji *et al.* [62] also offered a model for predicting the position of the catheter tip based on constant curvature assumption using multi-body dynamics framework.

Since the multi-body dynamic models reduce the degree of freedom of the system, the are computationally efficient but the accuracy is highly dependant on the resolution of the geometric discretization [118].

Particle Dynamics Models

Particle-based models (or mass-spring models) is mainly adopted for modeling the deformation of vasculature, catheters and guidewires [119, 120]. In this method, the catheter deformation is modeled through approximation of angular springs placed in between successive rigid links. In a

study [121], the catheter was modeled using particle dynamics model; while the vessels were assumed to be rigid and collision detection was assessed by gap volume technique [122]. Although the particle dynamics model have shown promising results in simplifying the computational complexity however it may lead to physically infeasible results [112]. As mentioned in [123] , the undesirable results can eventually end up in violation of the constant length assumption for guide wire- like structures.

Differential Geometric Models

Geometric modeling is a method in which the structure and its shape is defined by a set of specified number of points known as key points. The key points are not necessarily to be placed on the structure and could be located anywhere on the space (merely a mathematical entity). For instance a polynomial interpolation, piece-wise differentiable continuous (e.g., splines and B-splines) are used to represent the shape of the curve structure. Through defining the kinetic, potential (e.g. gravitational energy) and friction or viscoelastic energies combined with Lagrangian method, the equations of motion can be derived [116, 124]. In this respect, the final position of a guide wire was predicted by simulation the guide wire with a set of connected vertices [125]. The sets of vertices undergoes equal forced to model the guide wire (catheter). The equilibrium can be achieved having minimum energy constraint through iterating the solution. Recently, Hooshiar *et al.* [126] proposed and validated a non linear inverse Cosserat rod model for tip force estimation of the catheter.

Comparison

Despite the advantage of sensor- based haptic feedback systems such as less computational cost and shorter response time, current researches are mainly attracted to model- based haptic feed back. This is vastly due to the features that model- based approach offers to the scientist including: (1) less susceptibility to noise, (2) lower cost, (3) simple implementation,(4) easy plugging to the available robotic PCI systems, and (5) feasible application in surgical simulators [24, 105].

In choosing the most desirable model- based approach, there is always a compromise between the computational efficiency and accuracy [127]. Considering the vital role of continuity, conservation of momentum and conservation of energy in analysis catheter deformation [128], the continuum mechanics models used for the catheters and guide wires are the most accurate approach to be hired [111]. The most significant drawback of the model-based haptic feedback is the dependency of

the results to the mechanical properties of the catheter and cardiovascular structure [107]. Catheters are classified as hyper-redundant structures with respect to their deformations [129]. Hence, redundancy treatment method is required to enforce the solution to be converged to a favorable deformation. The method which is currently employed to tackle the hyper-redundancy of continuum robots is to impose geometric constraints regarding structure deflection [110], e.g. planar deflection [67], piece-wise constant curvature [130, 131] and constant radius curvature [132].

1.5 Contributions

To the best of author's knowledge, this study was the first study to propose a sensor-free tip-tissue contact force estimation schema for tendon-driven RFA catheter needless for tissue characteristics. In this study, first a novel vision- based approach for predicting the tip-tissue force contact was suggested. Afterwards, a new system design for incorporating the image-based force provision in the RCI systems was proposed. Next, learning- based approaches were incorporated to excel the performance of the force estimation system. Furthermore, each of the developed components was integrated with the proposed system design and their performances were assessed at the system level.In terms of knowledge dissemination, the following list summarizes the author's contributions during this master research:

(1) Pegah Yaftian, Naghmeh Bandari, Amir Hooshiar, and Javad Dargahi. "Image-based contact detection and static force estimation on steerable rfa catheters.", In 2020 International Conference on Biomedical Innovations and Applications (BIA), pages 57–60. IEEE, 2020 [133],

(2) Pegah Yaftian, Naghmeh Bandari and Javad Dargahi. " Comparison of Mechanistic and Learning-based Tip Force Estimation on Tendon-driven Soft Robotic Catheters.", In ACM/IEEE International Conference on Human-Robot Interaction (HRI), (Under review). IEEE, 2022 [134],

(3) Pegah Yaftian, Naghmeh Bandari, Amir Hooshiar and Javad Dargahi. "Real-time Intrinsic Tip Force Estimation on Tendon-driven Cathetersusing Tendon Tensions and Mechanistic

Modelling.", IEEE transactions on instrumentation and measurement, (Under review), 2021 [135].

1.6 dissertation layout

This thesis is prepared in manuscript-based style according to the "Thesis Preparation and Thesis Examination Regulations (version-2021) for Manuscript-based Thesis" of the School of Graduate Studies of Concordia University. It includes five chapters:

Chapter 1 provides the introductory materials, i.e., background, problem definition, objectives, literature review, and contributions.

Chapter 2 presents the proposed image-based contact force estimation and inverse kinematic- based model and the implemented solution schema as well as the validation studies.

Chapter 3 includes the system components, and the implementation methodology for force estimation of tendon driven catheters in combination with experimental validation studies for assessing the performance of the proposed and developed RCI system.

Chapter 4 is explored the alternatives for excelling the proposed method with learning algorithms. Also, the results of the validation studies are presented.

Chapter 5 summarizes the main contributions and achievements of this research. Moreover, the research limitations are acknowledged and potential future directions are provided.

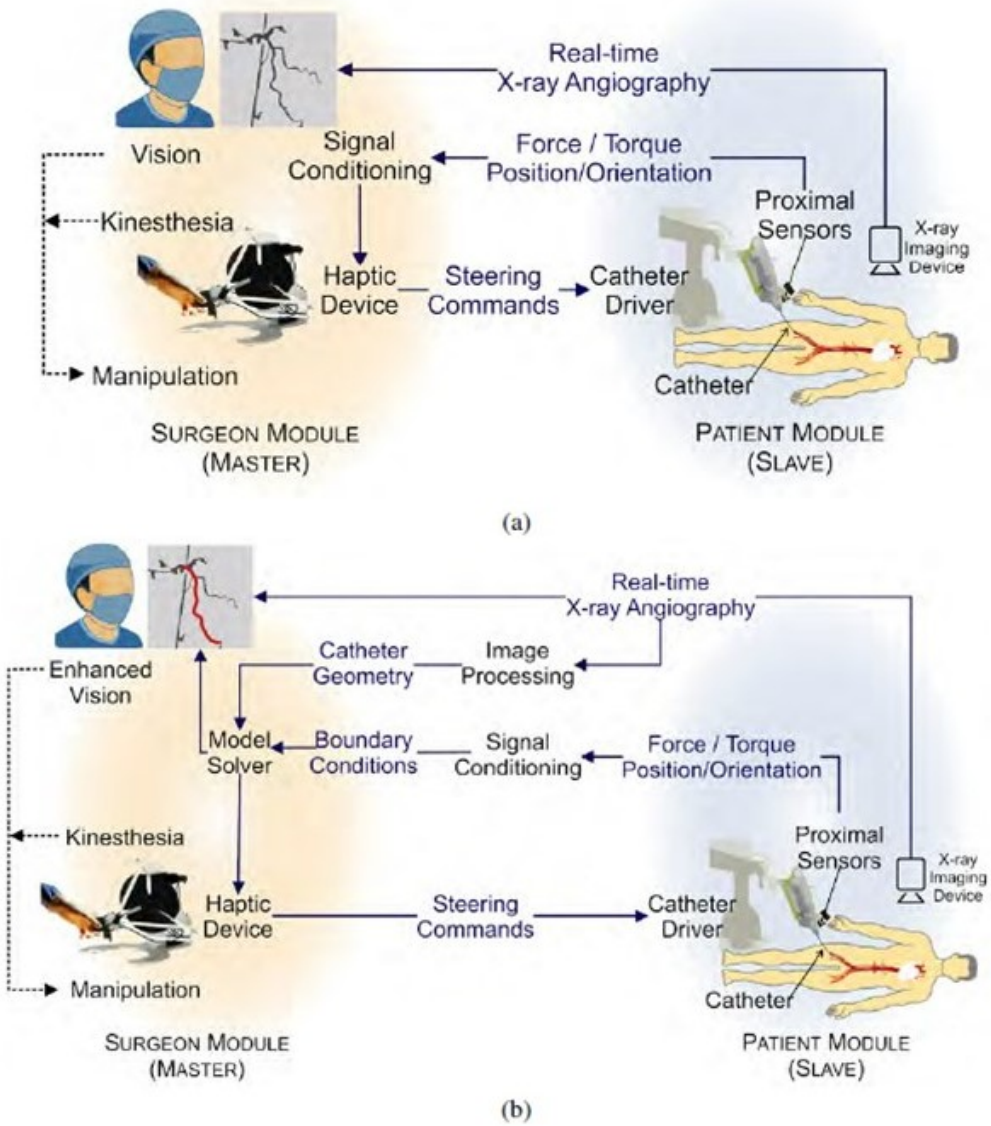

Figure 1.7: Haptic feedback provision in: (a) sensor-based and (b) model-based haptic feedback approaches [108]

Chapter 2

Image-based Contact Detection and Static Force Estimation on Steerable RFA Catheters

2.1 Abstract

Real-time force estimation is crucial for robot-assisted radio frequency ablation procedures to perform safe and effective treatment. This study proposes an image-based method real-time force estimation on steerable catheters. To this end, first a planar mechanical model of the catheter with an unknown contact force with the endocardium was developed. Afterward, an inverse solution schema based on the deformed shape of the catheter was proposed and verified. To validate the proposed method, finite element simulation was used to obtain deformed shape of a typical catheter with 0.5–5 N contact force. The results of the proposed image-based force estimation were in fair agreement with reference force used in finite element simulation. The relative estimation error was less than 5% for all forces and the goodness-of-fit between estimation and reference was $R^2 = 0.97$. The proposed method was in compliance with the acceptable accuracy and speed required for robot-assisted cardiac ablation procedures.

2.2 Introduction

trial fibrillation (AFib) is the most common arrhythmia in the elderly population in which the pulsation of cardiac electrical activity within the atria becomes chaotic. Consequently, the chaotic contraction of the atrium may result in blood clot and stroke [136]. Radio frequency ablation (RFA) is a minimally invasive surgical (MIS) approach to decrease the undesired pulsation within the cardiac tissue through partial burning of the arrhythmogenic sites.

To perform accurate and dexterous RFA, robot-assisted systems have been developed [24]. Studies have shown that maintaining a certain level of contact force between the tip of RFA catheters and the cardiac wall is necessary to obtain favorable clinical results [1, 32, 137]. Whereas, excessive contact force (>0.40N) increases the risk of tissue perforation and inadequate force (<0.1N) results in ineffective ablation. Fig. 2.1 shows a cardiac RFA catheter used for AFib treatment, schematically. Therefore, force control systems are an integral part of robot-assisted RFA procedures [138].

Researchers have proposed sensor-based [37] and model-based [24] contact force estimation schema for RFA catheters. Although the sensor-based studies have shown favorable accuracy, the main limitations of sensor-embedded catheters are size, weight, compromised flexibility, and high cost [139]. To avoid these limitations, model-based approach has recently gained momentum in the literature [24].

In an early effort, Khoshnam *et al.* [112],used a Pseudo Rigid-body (PRB) model for model-based force control of RFA catheters via the inverse solution of the catheter dynamics and image-based curvature analysis. However, this approach showed a low accuracy of 80%. Hasanzade *et al.* [107] used the piecewise circular arc for modeling the catheter. An iterative inverse solution was proposed in their study to estimate the contact force for the given shape of the catheter. Luo *et al.* [140] modeled the catheter as Kirchhoff elastic rod with contact detection between the catheter body and vascular anatomy obtained from a preoperative 3D reconstructed CT scan. Recently, Jolaei *et al.* [137] modeled the RFA catheters as spatial curves with constant bending curvature and successfully controlled the force at its tip using an artificial neural network (ANN)-based method for real-time force estimation [141]. However, the later approach requires an online detection of tissue characteristics through a generalized Kelvin-Voigt viscoelasticity modeling [1].

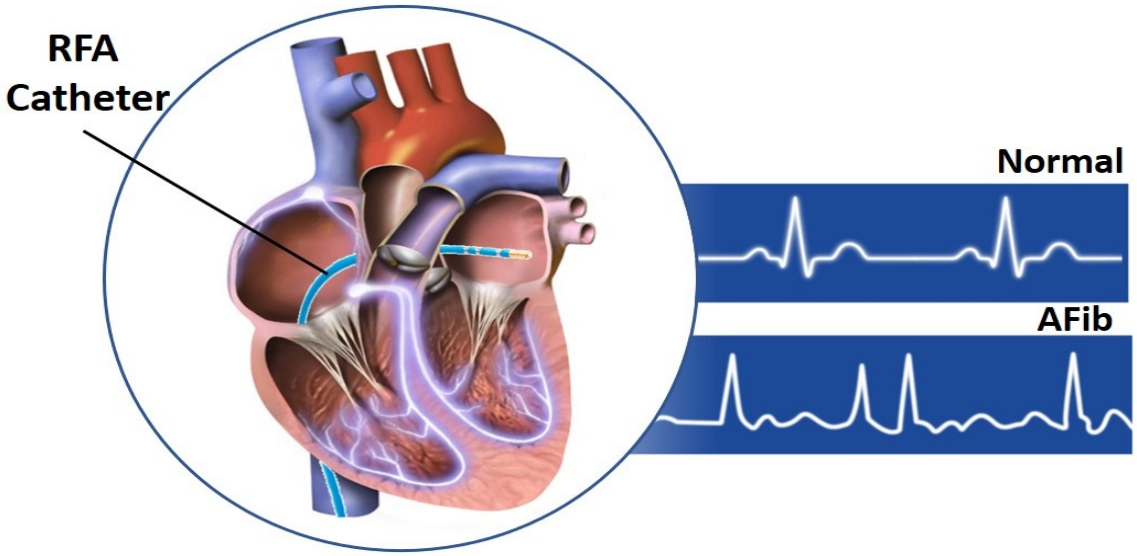

Figure 2.1: The schematic comparison of normal and chaotic pulsation with an RFA catheter

In this study, a force estimation framework based on real-time shape sensing of the RFA catheters was proposed and validated. The main contributions of this study are proposing a shape-based force estimation and semi-analytical solution of the inverse problem. Given the availability of real-time X-ray images during RFA procedures (fluoroscopy), the shape of the RFA catheter is available intra-operatively. The proposed force estimation is based on analytical shape reconstruction and inverse solution based on the catheter mechanics.

2.3 Material and Methods

2.3.1 Mechanical Model

Fig. 4.2 shows the free-body diagram (FBD) of a typical steerable catheter in contact with atrial tissue. The catheter is assumed of a straight initial shape. Typically, steerable RFA catheters are steered by a couple of agonist–antagonist cables which apply tensile force T_1 and T_2 to its tip. The cables are tangent to the body of the catheter along its length and are anchored to its tip with a separation of δ and apply a bending moment of $\mathbf{m}_{tip} = \begin{pmatrix} 0 & 0 & \delta(T_1 - T_2) \end{pmatrix}^T$ to the tip of the catheter. Also, the contact force between the catheter tip and atrial tissue is of the form $\mathbf{f}_{tip} = \begin{pmatrix} f_x & f_y & 0 \end{pmatrix}^T$.

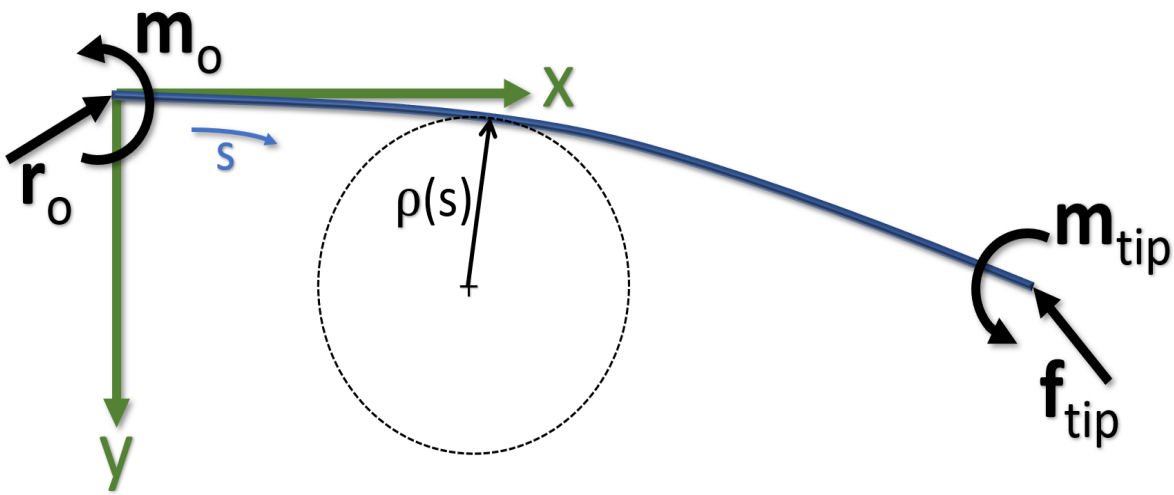

Figure 2.2: Free-body diagram of a deformed steerable catheter with contact force applied at its tip.

Kinematics

In this study the catheter is modeled as a curved line object with a length $L = 40$ mm and a diameter $D = 3$ mm (Fig. 4.2). These are typical catheter dimensions used in the literature, e.g. [137]. The length-to-diameter ratio of the catheter was larger than 10, thus, satisfied the small strain condition. Therefore, the catheter was modeled as an Euler–Bernoulli beam. The curve is parameterized with a continuous curve parameter $s \in [0, 1]$, where $s = 0$ and $s = 1$ correspond to the base and tip of the catheter, respectively.

Fig 4.2 shows the initial and deformed shape of the catheter. The deformed shape of the catheter was extracted from image-processing (Sec. 3.4.2) revealing $x = x(s)$ and $y = y(s)$ as continuous functions describing the shape of the catheter with respect to s. As stated in Sec. 3.4.2, the shape interpolation functions of $x(s)$ and $y(s)$ were polynomials of degree m and n, respectively:

$$x(s) = \sum_{i=0}^{m} a_i s^i, \quad y(s) = \sum_{j=0}^{n} b_j s^j, \tag{1}$$

which resulted in radius of curvature of the form:

$$\rho(s) = \frac{((\sum_{i=1}^{m-1} i a_i s^{i-1})^2 + (\sum_{j=1}^{n-1} j b_j s^{j-1})^2)^{\frac{3}{2}}}{\sum_{j=2}^{n-1} j(j-1) b_j s^{j-2}} \tag{2}$$

Static Equilibrium

The force and moment equilibrium equations at any arbitrary point along of the catheter determined by s are:

$$\mathbf{r}_\circ + \mathbf{f}(s) = \mathbf{0}, \tag{3}$$

$$\mathbf{m}_\circ + \mathbf{m}(s) + \begin{pmatrix} x(s) & y(s) & 0 \end{pmatrix}^T \times \mathbf{f}(s) = \mathbf{0}. \tag{4}$$

where, $\mathbf{r}_\circ$ and $\mathbf{m}_\circ$ are constant reaction force and moment vectors at base, $\mathbf{m}$ is the internal bending moment, and $\mathbf{f}$ is the internal force vector. By applying the boundary condition at $s = 1$, where $\mathbf{m}(s)|_{s=1} = \mathbf{m}_{tip}$ and $\mathbf{f}(s)|_{s=1} = \mathbf{f}_{tip}$, the base reactions were determined as:

$$\mathbf{r}_\circ = \begin{pmatrix} -f_x & -f_y & 0 \end{pmatrix}^T, \tag{5}$$

$$\mathbf{m}_\circ = \begin{pmatrix} 0 & 0 & \delta(T_2 - T_1) - x(1)f_y + y(1)f_x \end{pmatrix}^T. \tag{6}$$

Therefore, at any s, the z-component of $\mathbf{m}(s)$ is:

$$m_z(s) = \delta(T_1 - T_2) + \begin{pmatrix} x(1) - x(s) & y(1) - y(s) \end{pmatrix} \begin{pmatrix} f_y \\ -f_x \end{pmatrix} \tag{7}$$

On the other hand, Euler–Bernoulli beam theory shows that for planar slender beams:

$$m_z(s) = \frac{EI}{\rho(s)}, \tag{8}$$

where, EI is the flexural rigidity of the beam.

Inverse Solution

The coefficients a_i and b_j determine the shape of the deformed catheter and are obtained from image-processing. By assuming T_1 and T_2 as *a-priori* knowledge, derived from input tensions by the user, the right-hand-side of Eq. 7 and Eq. 8 shall necessarily be equal for any and all given $s = s_\circ$. Therefore, the force estimation problem is defined as a minimization problem to find f_x

and f_y which minimizes the residual absolute error Γ defined as:

$$\text{minimize} \quad \Gamma = |m_z(s) - \frac{EI}{\rho(s)}|, \tag{9}$$

for any and all given $s \in [0, 1]$. In a special case that the catheter is not in contact with tissue, $f_x = f_y = 0$, the residual function becomes constant and the minimization problem reveals a trivial result of zero contact force. This is a physically plausible solution as it corresponds to a single curvature deformation and is in compliance with Eq. 8 with constant $\rho = \text{const}$.

For numerical solution of deformation with non-zero contact force, the catheter was discretized in 9 sections and Eq. 9 was evaluated for $s = 0.1, 0.2, \cdots, 0.9$. Eventually Eq. 9 was re-ordered as:

$$\mathbf{A} \begin{pmatrix} f_x \\ f_y \end{pmatrix} - \mathbf{B} = 0, \tag{10}$$

Where,

$$\mathbf{A} = \begin{pmatrix} x(1) - x(0) & y(0) - y(1) \\ \vdots & \vdots \\ x(1) - x(0.9) & y(0.9) - y(1) \end{pmatrix}, \mathbf{B} = - \begin{pmatrix} \delta(T_1 - T_2) - \frac{EI}{\rho(0)} \\ \vdots \\ \delta(T_1 - T_2) - \frac{EI}{\rho(0.9)} \end{pmatrix}. \tag{11}$$

It is noteworthy that the components of matrix **A** are merely obtained from the image-based shape extraction and represent the deformation, while the components of vector **B** contain the steering tensions T_1 and T_2 and local curvature of the catheter at equidistant sample locations.Based on Moore-Penrose pseudo-inverse theorem, the solution to Eq. 10 which is unique and is necessarily the solution to the proposed norm-minimization problem is:

$$\begin{pmatrix} f_x & f_y \end{pmatrix}^T = (\mathbf{A}^T\mathbf{A})^{-1}\mathbf{A}^T\mathbf{B}. \tag{12}$$

This inverse solution reveals the external force f_x and f_y through knowledge of the deformation (image-processing) and mechanical properties of the catheter. The flexural rigidity of the catheter modeled in this study was set to $EI = 723.7$ MPa.mm^4 [137].

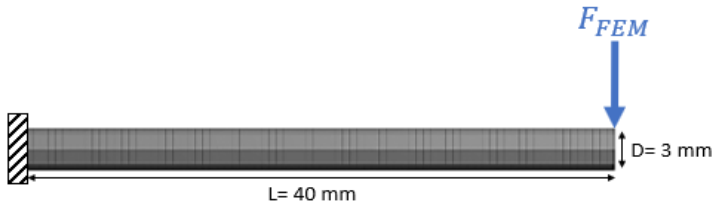

(a)

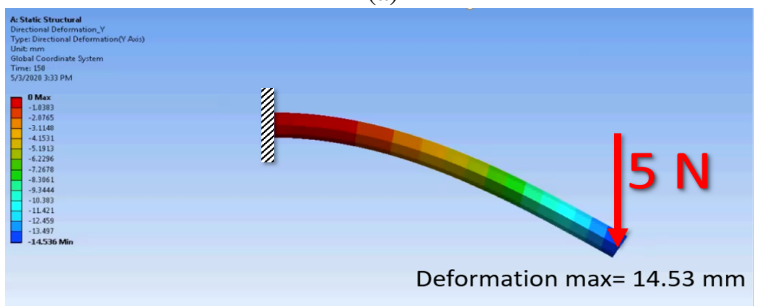

(b)

Figure 2.3: (a)Mesh quality and dimensions of the catheter distal shaft, (b)Finite Element Model(FEM) of the catheter curvature upon the application of the external force.

2.4 Validation Study

In order to validate the proposed image-based method, the force estimation was performed on the results of finite element (FE) analysis of a similar catheter under concentric horizontal force at its tip. The image-processing and inverse solution was implemented in Matlab 2019b (Mathworks, MA, USA) the FE simulations were run in Ansys Workbench v17 (Ansys Inc., PA, USA).

2.4.1 Finite Element Simulation

Fig. 2.3(a) shows the FE model solved in this study. The model was solved with nonlinear geometry (large deformation) assumption and had 51 nodes and 50 linear bending elements. Homogeneous Dirichlet and Neumann boundary conditions were applied at the left-most node of the model to simulate the cantilever condition. A vertical concentrated force of 0.5–5 N magnitude was applied to the right-most node in separate simulations. Fig. 2.3(b) shows the representative deformed shape of the catheter under 5 N.

2.4.2 Image-based Deformation Extraction

To extract the shape of catheter, first each image was converted to gray-scale and thresholded manually to obtain a binary map of the pixels belonging to the catheter. Afterward, the centerline of the extracted shape (1-pixel width) was obtained through averaging the vertical white pixels, i.e., pixels with *'1'* value. Fig. 2.4(a) shows the binary map and the extracted centerline of Fig. 2.3(b). The parameter s was defined for each individual pixel on the centerline as:

$$s_i = \frac{\sum_{k=1}^{i} \sqrt{(x_k - x_{k+1})^2 + (y_k - y_{k+1})^2}}{L} \quad i = 1 \cdots p-1, \tag{13}$$

Where, p was the total number of pixels constructing the centerline, x and y were the horizontal and vertical position of the pixel in the image in millimeters. Next, to obtain coefficients of the shape interpolation functions introduced in Eq. 1, an iterative curve-fitting was performed on $< s_i, x_i >$ and $< s_i, y_i >$ ordered 2-tuples. The curve-fitting was stopped once the goodness-of-fit would surpass a minimum $R^2 \geq 0.97$. Fig. 2.4(b)–(c) show the $x(s)$ and $y(s)$ for the deformed shape of catheter under 5 N load, respectively as a representation.

2.5 Result and Discussion

Fig. 2.5 depicts the deformed shape of catheter for tip forces of 0.5–5 N. The maximum displacement was for 5 N force with 14.53 mm in y-direction. Since the maximum deflection is more than 10% of the length of the beam (small deformation condition for Euler–Bernoulli beams), the large deformation assumption is confirmed. The proposed force estimation method in Sec. 2.3.1 was applied on the results of FE simulations. Table 2.1 summarizes the force estimation results.

The maximum estimation error was 3.9% for 5 N force, while the maximum estimation error for force below 2 N was 3.8%. In all the load cases the force estimation error was below 5% (Fig. 2.6(a). Also, the results showed a strong correlation between the reference force (FE) and the image-based estimations (R^2=0.97). The trend of estimation error was decreasing for 0.5–2 N and increasing afterward. The reason was related to the combination of the image resolution and large-deformation effects. More specifically, at small forces ($\leq$ 2 N) the deflection of parts of the

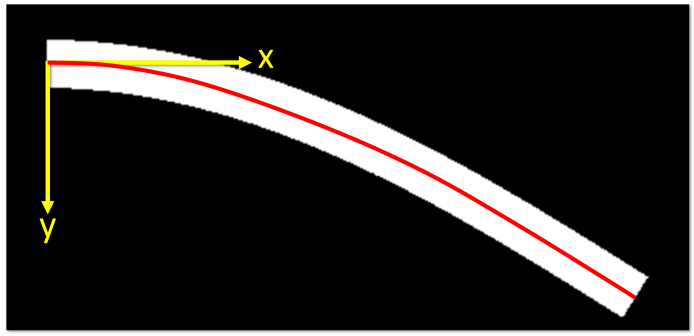

(a)

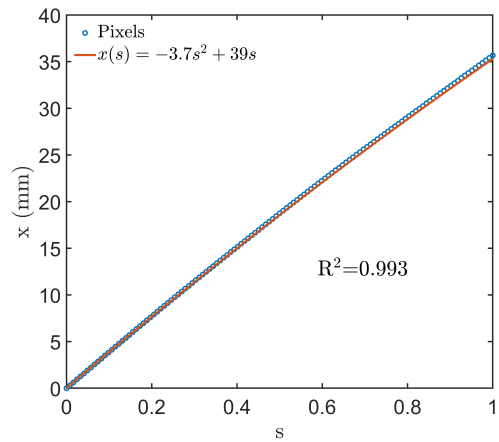

(b)

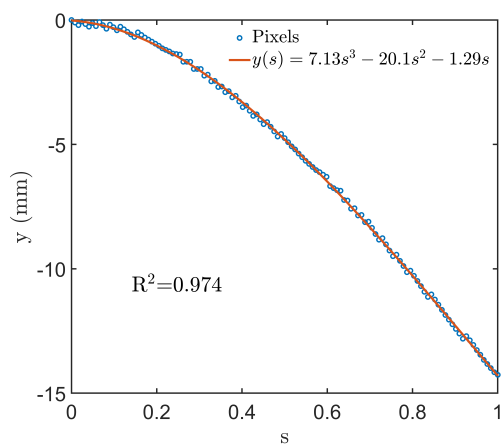

(c)

Figure 2.4: (a) Extracted deformed shape of the catheter, (b) x-interpolation, and (c) y-interpolation of the shape of the deformed catheter.

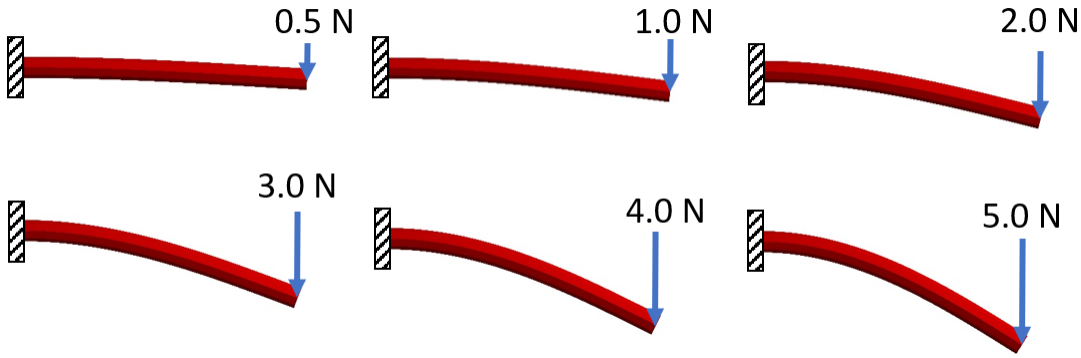

Figure 2.5: Catheter deformation extracted from FE simulation for 0.5–5 N.

Table 2.1: Results of the FE simulations and the force estimation.

Ref. F_{tip} (N)	**Image-based F_{tip}** (N)	**Abs. Error** (N)	**Rel. Error** $\times$ 100 (%)
0.5	0.483	(-) 0.0175	3.8%
1	0.992	(-) 0.008	0.8%
2	2.004	(+) 0.004	0.2%
3	3.051	(+) 0.051	1.7%
4	4.128	(+) 0.128	3.2%
5	4.805	(-) 0.805	3.9%

catheter is comparable to the width of a single pixel in the image and is not detected by the image processing. By increasing the force ($\leq$ 2 N) the large deformation effect causes a non-negligible tangential component for the tip force,along the catheter tip, and causes longitudinal stress and deformation. The resulted stress and deformation along the catheter curvature can not be captured by the Euler–Bernoulli theory. Furthermore, the computation time of the proposed method per image was 6 ± 3 ms, which corresponds to a minimum of 111 Hz refresh-rate. Given that the frame-rate of the commercially available X-ray imaging machines is typically less than 30 Hz, the computational performance of the proposed method fits the requirement for real-time surgical applications.

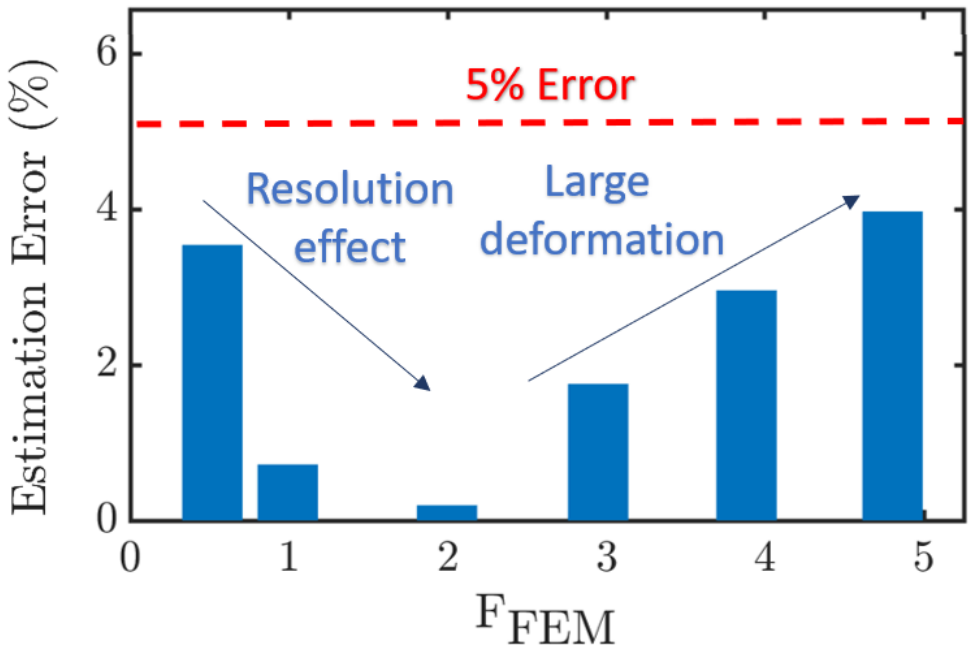

Figure 2.6: Change in the estimation error with respect to force magnitude.

2.6 Conclusion

The objective of this study was to propose and validate an image-based force estimation for steerable catheters. To this end, initially a shape-based force sensing method was proposed. Having validated the proposed method, different curvatures of a typical catheter were extracted from the FE simulation to be used for force sensing.the validation study results showed acceptable accuracy and computational performance of the proposed image-based force estimation technique for surgical applications. For future studies, dynamic modeling of the catheter and extension of the planar model to the 3D model are planned. Moreover, experimental validation of the proposed force estimation method with video camera integration for simulating more realistic conditions will be studied.

Chapter 3

Real-time Intrinsic Tip Force Estimation on Tendon-driven Catheters using Tendon Tensions and Mechanistic Modelling

3.1 Abstract

Tip contact force estimation is a clinical need for tendon-driven catheters used in radio-frequency ablation procedures. In this study, a mechanistic tip force estimation method based on tendon tension and mechanical model of the catheter was proposed and validated. To this end, first a parameterized shape sensing method was proposed and used to interpolate the deformed shape of the catheter in real-time. Next, a mechanistic model of the catheter with large deformation was developed. Afterward, the unknown tip force was estimated using a semi-analytical approach with a fast solver. The proposed method was tested on three different polymeric tissue phantoms with various mechanical properties. Also, the method was tested on porcine atrial tissue to exhibit its accuracy and independence from tissue properties. The maximum root-mean-square error of the force

estimation was 0.0091 N, 0.0080 N, and 0.0072 N for slow, fast, and manual tests on tissue phantoms while it was 0.01 N, 0.009 N, and 0.012 N for the tests on the porcine atrial tissue. For both validation test series, the estimated force and ground truth show acceptable linearity in correlation diagrams.

3.2 Introduction

3.2.1 Background

Catheter-based ablation therapy is currently the gold-standard treatment of atrial fibrillation (AFib) [142]. AFib is a state that the heart beats with irregular pattern, mainly due to the undesired electrical discharges originating from the pulmonary veins [142,143]. The majority of ablation therapies are performed with a radiofrequency ablation (RFA) approach. During RFA, radiofrequency wave from the catheter tip induces an electrical current in the atrial tissue, resulting in irreversible thermal damage to the unwanted tissue, thus making it non-conductive. The non-conductive parts in the atrial tissue further blocks the electrical current shunt from the pulmonary vein areas to the atrium, thus, reduces the magnitude of arrhythmia [14]. Fig. 4.1 depicts the schematic configuration of an RFA catheter inside the heart's right atrium.

Studies have shown that the success of RFA depends on maintaining an optimal catheter tip force during the RFA, i.e., 0.1 N to 0.3 N [24,32,144]. To this end, the use of force sensing catheters have expanded in the last decade. Such catheters are used for intraoperative monitoring of the tip contact force on RFA catheters. Clinical studies have shown that the use of force sensing catheters can reduce the recurrence rate of RFA procedures from 50% to 30% [145–147]. For better navigation and access to the inferior and posterior walls of the atria, steerable catheters have been integrated with force sensors. Steerable catheters typically have a tendon-driven actuation mechanism with a set of agonist-antagonist tendons supported by a flexible backbone. [148,149]. Nevertheless, embedding force sensor in the steerable catheters has compromised their flexibility. Moreover, the sensor embedded catheters are typically ten-times more expensive than the conventional catheters, which has limited their affordability at large scale. Therefore, there is a clinical gap for a sensorless modality

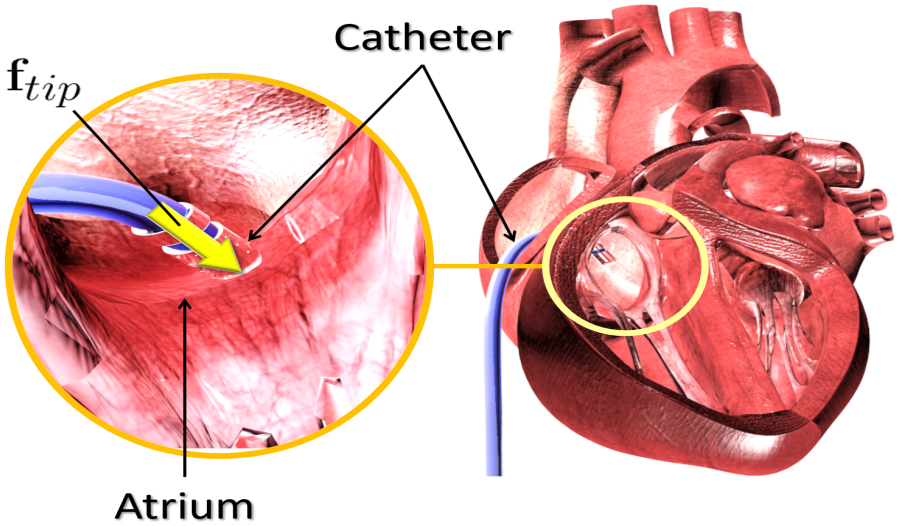

Figure 3.1: Schematic configuration of an RFA catheter inside the right atrium.

need to be filled for intraoperative contact force monitoring. In view of the limitations of the existing force sensing catheters, a sensorless force estimation framework for steerable tendon-driven catheters was proposed and validated in this study. To this end, a mechanistic model of the tendon-driven catheters was developed to adapt our previous image-based force estimation methodologies to tendon-driven catheters, e.g., [126, 133].

3.2.2 Related studies

To model the mechanics of steerable catheters, two modelling approaches have been proposed in the literature: model-based and model-free (heuristic) approach. In the model-based approach, a mechanistic model is derived to model the catheter deflection as a deformable continuum robot subjected to tip bending moment and tip forces. In this regard, studies have proposed formulations based on continuum mechanics, [26], differential geometry [126, 150], multi-body dynamics [151], and particle-based dynamics [152].

For heuristic modelling, various data-driven regression models such as artificial neural network (ANN) [144] and Gaussian process modelling (GPM) [153] have been investigated. Despite the relative simplicity, researchers have been more motivated to explore mechanistic models as the

medical applications require high precision, repeatability, and stability [24]. For force estimation of tendon-driven catheters, typically the inertia of the catheter is neglected justified by its relatively small mass. Therefore, the majority of representative studies have modelled the catheters under quasi-static condition [154, 155]. From a kinematics point of view, the continuum tendon-driven catheters are under-actuated and have infinite degrees-of-freedom (DOFs). Adopting approximation assumptions, such as piecewise constant curvature (PCC), single-plane bending, and constant bending curvature,infinite DOFs have been reduced and derived the kinematics thereof. For example, the PCC-based kinematic model, proposed in [115], was employed by Ganji *et al.* [62] to approximate the deformations of a commercial tendon-driven catheter with high computational efficiency. Because of using a rigid serial arm modelling approach, the modelling error was relatively high in [62]. A similar kinematic model with three circular arcs was proposed in [107] and the catheter was modelled as an *elastica* with large deformation. Despite its accuracy in tip position prediction under various tip forces, this model was highly sensitive to the accuracy of the image-based shape approximation and exhibited high force estimation errors.

In a recent study, Hooshiar *et al.* [26] proposed an inverse finite-element method with Euler-Bernoulli beam type for force estimation along endovascular devices. They used a polynomial-base shape interpolation for shape sensing. Despite its computational efficiency, their method merely considered lateral forces along the catheter and did not include tip forces and tip moments. Other flavors of finite element-based methods, e.g., finite element Cosserat rod [156], have been also proposed in the literature. Nevertheless, finite element-based methods generally suffer from computational efficiency for real-time applications [24]. Another limitation of the finite element-based methods is that they intrinsically require discrete nodal positions for optimization-based force estimation while accurate shape approximation methods are typically continuous. In a recent study, Jolaei *et al.* [1, 157] adopted a generalized Kelvin-Voigt viscoelastic model to estimate catheter tissue contact force based on catheter tip indentation into the tissue. Despite the high accuracy of the displacement-based method for force control of RFA catheters, it mandates a real-time tissue characterization schema which might be prone to non-negligible error or natural variability due to the heterogeneous mechanical properties of the atrial tissue. In a recent study, Donat *et al.* [158] proposed an accurate image-based tip force estimation for a flexible continuum arm using the deep

direct cascade learning (DDCL) method. However, their proposed methodology was based on training a statistical model with simulation data and re-training with real-world data which may suffer from generalization problem because of the variability of the design between different catheters.

3.3 contributions

The main contributions of this study are:

(1) image-based shape sensing with continuous polynomial shape interpolation functions,

(2) derivation of the kinematics of the tendon-driven catheter as a continuum robot based on continuous polynomial shape,

(3) derivation of balance equations employing the proposed kinematics,

(4) proposing a fast optimization-based tip force estimation schema, and

(5) ex-vivo validation of the proposed force estimation framework.

In the following, Sec. 3.4 summarizes the shape sensing, derivation of the kinematics, balance equations, and force estimation, Sec. 3.5 summarizes the objectives, protocols, and the key findings of two validation studies, and Sec. 3.6 provides the concluding remarks, limitations of the study, and future directions.

3.4 Methodology

In this section, a description of the catheter fabrication and the developed system are provided. Afterward, the inverse kinematics of catheter based on Euller Bernoulli's assumption combined with image-based analysis is obtained. The validity of the proposed method was previously investigated using FEM analysis [133].In the end, the experimental test procedures and setups for study the proposed force estimation method are outlined.

3.4.1 Catheter Prototype

The tendon-driven catheter was fabricated with two inextensible tendons attached to two antipodal points of the catheter tip. The diameter and length of the catheter were chosen to be 6 mm and 40 mm, respectively. The selected dimensions matched the use of a 18-Fr catheter and the average transversal diameter of the right atrium [159, 160].

The catheter is comprised of a flexible body and an integrated steel compression coil spring. For fabricating the main body of the catheter, a cylindrical mold was rapid prototype with 3D printer (Replicator+; MakerBot, NY). The coil spring with 5 mm of nominal outer diameter and 0.35 N/mm of compressive stiffness, was integrated within the cylindrical mold. Afterwards the mold was filled with silicon rubber material (Ecoflex™00-30; Smooth-on, Inc., PA) and degassed in a vacuum chamber (Best Value Vacs, IL) under 29 mmHg vacuum pressure for a homogeneous texture of catheter body. Compensating for the viscous energy damping, the coil spring would facilitate recovering catheter original shape in presence and absence of a force at its tip. For further curing, the mold was rested for 24-48 hours in room temperature (25 °C).

3.4.2 Shape Sensing

This section starts with observing the change in the catheter curvature when it is exposed to an external force or moves in free space. An image captured by the camera is shown in Fig. 3.2(a). According to Hannan *et al.* [161] for determining a curvature of continuum robots manipulator identifying three points is sufficient. As a matter of fact, a custom algorithm was used to find a curve representing the catheter configuration. In this regard, each image was converted to a gray-scale image, thresholeded and finally converted to a binary map of pixels to find the center of the tip (Fig. 3.2(b)-(c)). Afterward, the right-most point of the catheter where catheter intersects with the catheter holder was manually detected (Fig.3.2(d)).The third point was assumed to be the center of the circle which the catheter curvature is assumed to be a portion of that. Herein, the curve, located at the center line of the catheter, successfully represents the catheter curvature as shown in Fig.3.2(f). Detecting the location of center line pixels, the parameter s was defined for each

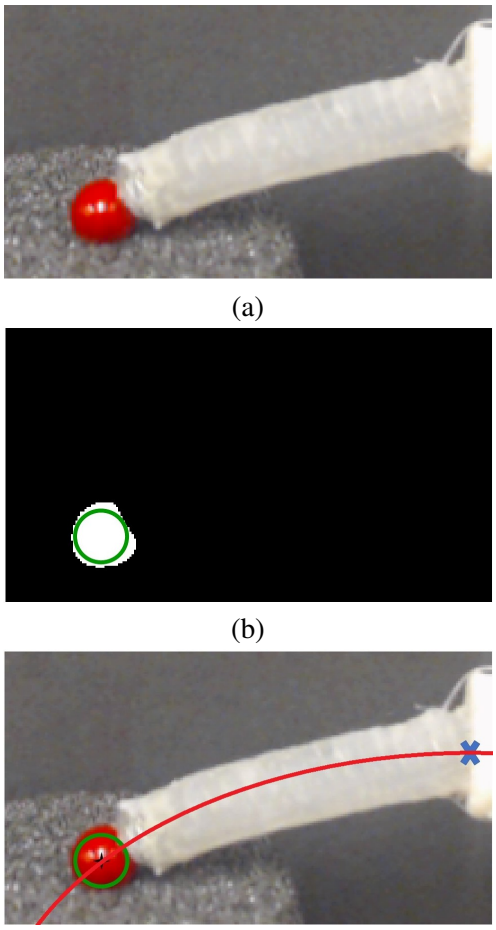

(a)

(b)

(c)

Figure 3.2: (a) Raw image of the deflected catheter, (b) binary image of the catheter with the identified tip center, (c) circular arc fitted to the backbone of the catheter.

individual pixel on the cente rline as:

$$s_i = \frac{\sum_{k=1}^{i} \sqrt{(x_k - x_{k+1})^2 + (y_k - y_{k+1})^2}}{L} \quad i = 1 \cdots p - 1, \tag{14}$$

where, p was the total number of pixels introducing the center line, the horizontal and vertical locations of pixels were represented with x and y in millimeters. Next, to obtain coefficients of the shape interpolation functions in Eq. 15, an iterative curve-fitting was performed on $< s_i, x_i >$ and $< s_i, y_i >$ ordered 2-tuples. The curve-fitting was stopped once the goodness-of-fit would reaches a minimum $R^2 \geq 0.97$.

3.4.3 Tendon Tension

Motor Current Measurement

RCI system requires a control framework to perform motor current feedback and eventually force feedback at the tip of the catheter; the proposed control system is presented in figure 3.6. The ultimate goal of control system is to estimate and maintain a force through applying a PID controller to the motor currents and catheter curvature analysis.Afterward, the control system would determine the desired current for motors to generate the desired force at the tip of the catheter. The formulas are extensively explained in the inverse kinematic section.

Torque Constant Identification

As mentioned in 3.5.1, estimating the force at the catheter tip necessitates finding the motor constant (K_m) indicating the linear relation between the tendon tension and motor current. Fig.3.3 shows the developed setup for investigating the motor constant which consists of a Phidget DC motor and a current sensor for recording the motor currents in real-time, a pulley with a 20mm diameter was attached to the motor shaft and the tendon was wrapped around it. Moreover, to increase the tendon's compliance and avoiding rapid rise in the tendon tension, a spring coil was attached in the middle of the tendon. The tendon was terminated on an ATI Mini40 force sensor (ATI Inc., NC, USA) to record the total tensile force. The motor was run clockwise and counterclockwise directions under current control within 80% of its nominal current rating (1000 mA), i.e., 100–900 mA. This test procedure was repeated three times.

Fig. 3.3 depicts the variation of tensile force in the tendon with the motor's current. Linear regression among the three repetitions showed a goodness-of-fit of 99% and with $K_m = 0.0169\frac{\text{mNm}}{mA}$.

3.4.4 Mechanical Model

The free body diagram of a steerable catheter in contact with cardiac tissue is depicted in Fig. 3.5. A typical steerable catheter is steered by a couple of agonist–antagonist tendons which apply tensile force T_1 and T_2 to its tip. The catheter is assumed to have no bending at the initial state when

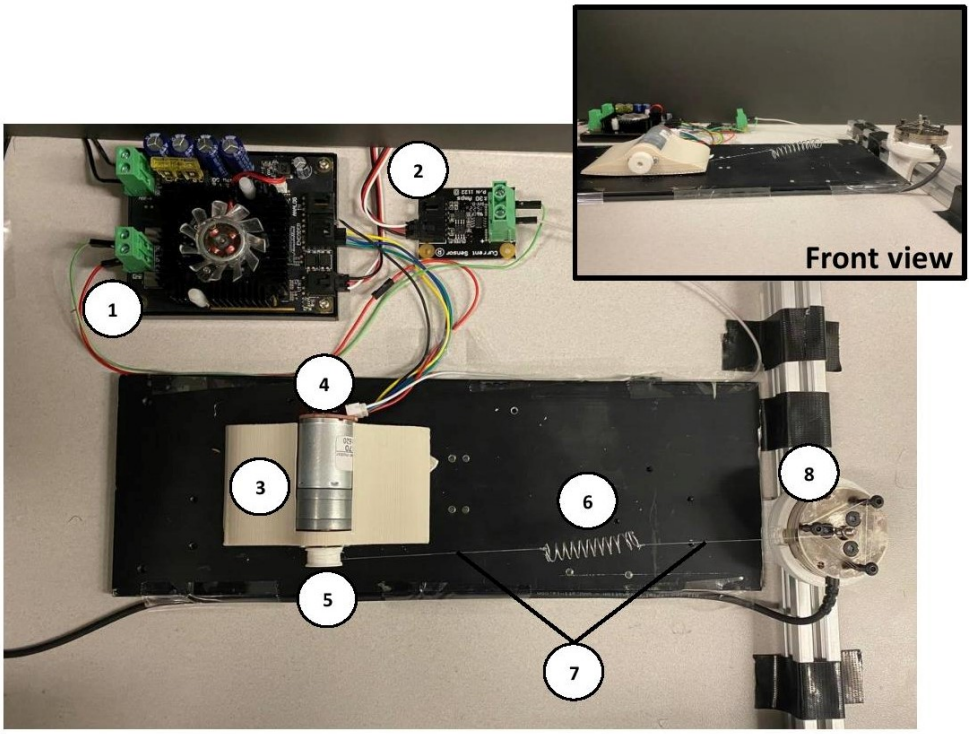

1. DC motor Phidget (DC motor controller)
2. Current Sensor
3. Motor holder
4. DC motor
5. Pulley
6. Coil spring
7. Tendons
8. Force sensor

Figure 3.3: Components of the developed setup for finding the DC motor constant

it has no contact with atrial tissue. As shown, the cables are tangent to the body of the catheter and hinged to its tip with a distance equals to tip diameter (δ). The bending moment and contact force at the tip of the catheter are in the form of $\mathbf{m}_{tip} = \begin{pmatrix} 0 & 0 & \delta(T_1 - T_2) \end{pmatrix}^T$ and $\mathbf{f}_{tip} = \begin{pmatrix} f_x & f_y & 0 \end{pmatrix}^T$, respectively.

Kinematics

Since the ratio of the length to diameter of the fabricated catheter is considerably large, the small strain condition can be satisfied. Hence, the catheter was modelled based on Euler–Bernoulli beam theory. The catheter curvature was also assumed to be a section of a circular shape; so when it is in initial straight state the diameter of circle which the catheter is a part of that, is infinite. The curve is parameterized with a continuous curve parameter $s \in [0, 1]$, where $s = 0$ and $s = 1$ correspond

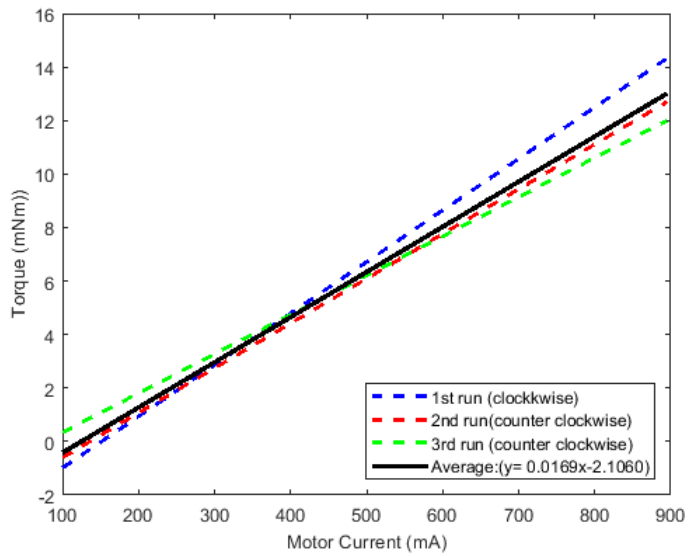

Figure 3.4: Linear relation of motor current and motor torque result from experiments.

to the leftmost point of the catheter (base) and the rightmost end of the catheter (tip), respectively. Fig 3.5 shows the deformed shape of the catheter. The curvature of the catheter was extracted from image-processing technique in real- time. The technique for image extraction of the catheter was explicitly explained in (Sec. 3.4.2). As stated in Sec. 3.4.2, the shape interpolation functions of $x(s)$ and $y(s)$ were polynomials of degree m and n, respectively:

$$x(s) = \sum_{i=0}^{m} a_i s^i, \quad y(s) = \sum_{j=0}^{n} b_j s^j, \tag{15}$$

which resulted in radius of curvature of the form:

$$\rho(s) = \frac{((\sum_{i=1}^{m-1} i a_i s^{i-1})^2 + (\sum_{j=1}^{n-1} j b_j s^{j-1})^2)^{\frac{3}{2}}}{\sum_{j=2}^{n-1} j(j-1) b_j s^{j-2}} \tag{16}$$

Balance Equations

The force and moment equilibrium equations at any arbitrary point along of the catheter determined by s are:

$$\mathbf{r}_\circ + \mathbf{f}(s) = \mathbf{0}, \tag{17}$$

$$\mathbf{m}_\circ + \mathbf{m}(s) + \begin{pmatrix} x(s) & y(s) & 0 \end{pmatrix}^T \times \mathbf{f}(s) = \mathbf{0}. \tag{18}$$

Where, $\mathbf{r}_\circ$ and $\mathbf{m}_\circ$ are constant reaction force and moment vectors at base, $\mathbf{m}$ is the internal bending moment, and $\mathbf{f}$ is the internal force vector. By applying the boundary condition at $s = 1$, where $\mathbf{m}(s)|_{s=1} = \mathbf{m}_{tip}$ and $\mathbf{f}(s)|_{s=1} = \mathbf{f}_{tip}$, the base reactions were determined as:

$$\mathbf{r}_\circ = \begin{pmatrix} -f_x & -f_y & 0 \end{pmatrix}^T, \tag{19}$$

$$\mathbf{m}_\circ = \begin{pmatrix} 0 & 0 & \delta(T_2 - T_1) - x(1)f_y + y(1)f_x \end{pmatrix}^T. \tag{20}$$

Therefore, at any s, the z-component of $\mathbf{m}(s)$ is:

$$m_z(s) = \delta(T_1 - T_2) + \begin{pmatrix} x(1) - x(s) & y(1) - y(s) & 0 \end{pmatrix} \begin{pmatrix} f_y \\ -f_x \\ 0 \end{pmatrix} \tag{21}$$

On the other hand, Euler–Bernoulli beam theory shows that for planar slender beams:

$$m_z(s) = \frac{EI}{\rho(s)}, \tag{22}$$

where, EI is the flexural rigidity of the beam.

3.4.5 Force Estimation

The coefficients a_i and b_j determine the shape of the deformed catheter and are obtained from image-processing. By assuming T_1 and T_2 as *a-priori* knowledge, derived from input tensions by the user, the right-hand-side of Eq. 21 and Eq. 22 shall necessarily be equal for any and all given

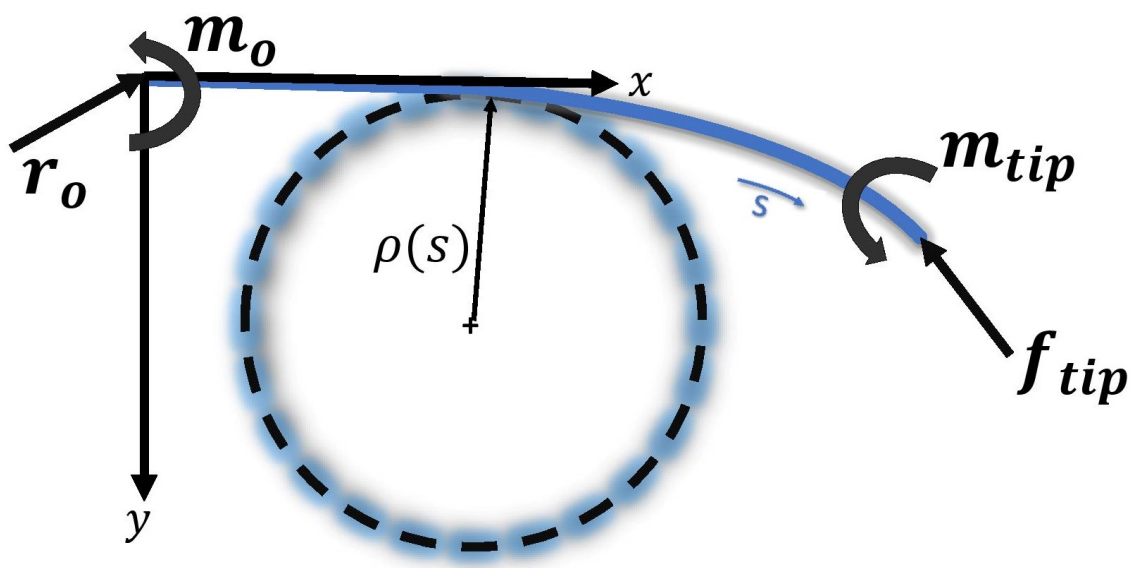

Figure 3.5: Free-body diagram of a deformed steerable catheter with contact force applied at its tip.

$s = s_\circ$. Therefore, the force estimation problem is defined as a minimization problem to find f_x and f_y which minimizes the residual absolute error Γ defined as:

$$\text{minimize} \quad \Gamma = |m_z(s) - \frac{EI}{\rho(s)}|, \tag{23}$$

for any and all given $s \in [0, 1]$. In a special case that the catheter is not in contact with tissue, $f_x = f_y = 0$, the residual function becomes constant and the minimization problem reveals a trivial result of zero contact force. This is a physically plausible solution as it corresponds to a single curvature deformation and is in compliance with Eq. 22 with constant $\rho = \text{const}$.

For numerical solution of deformation with non-zero contact force, the catheter was discretized in 9 sections and Eq. 28 was evaluated for $s = 0.1, 0.2, \cdots, 0.9$. Eventually Eq. 28 was re-ordered as:

$$\mathbf{A} \begin{pmatrix} f_x \\ f_y \end{pmatrix} - \mathbf{B} = 0, \tag{24}$$

Where,

$$\mathbf{A} = \begin{pmatrix} x(1) - x(0) & y(0) - y(1) \\ \vdots & \vdots \\ x(1) - x(0.9) & y(0.9) - y(1) \end{pmatrix}, \mathbf{B} = - \begin{pmatrix} \delta(T_1 - T_2) - \frac{EI}{\rho(0)} \\ \vdots \\ \delta(T_1 - T_2) - \frac{EI}{\rho(0.9)} \end{pmatrix}. \quad (25)$$

It is noteworthy that the components of matrix **A** are merely obtained from the image-based shape extraction and represent the deformation, while the components of vector **B** contain the steering tensions T_1 and T_2 and local curvature of the catheter at equidistant sample locations.Based on Moore-Penrose pseudo-inverse theorem, the solution to Eq. 29 which is unique and is necessarily the solution to the proposed norm-minimization problem is:

$$\begin{pmatrix} f_x & f_y \end{pmatrix}^T = (\mathbf{A}^T\mathbf{A})^{-1}\mathbf{A}^T\mathbf{B}. \quad (26)$$

This inverse solution reveals the external force f_x and f_y through knowledge of the deformation (image-processing) and mechanical properties of the catheter. The flexural rigidity of the catheter modeled in this study was set to $EI = 723.7$ Nmm^2 [144].

3.5 Validation Studies

3.5.1 Study I: Force Estimation on Tissue Phantoms

Tissue phantoms and characterization

To evaluate the performance of the proposed force estimation framework, the system was tested on three different tissue phantoms, i.e., sponge (Tissue-1), polymeric soft tissue (Tissue-2), and polymeric extra soft tissue (Tissue-3) depicted in Fig. 3.7(a). Three tissue phantom samples were tested under uniaxial compression condition using a universal testing machine (ElectroForce 3200, TA Instruments, DE, USA). The tests were performed under sinusoidal compression with a 20% compressive strain. Fig. 3.7(a) shows a representative view of the test setup and Fig. 3.7(c) depicts the average force-displacement diagram of the three tissue phantoms. The force-displacement data

were fitted by a two-term Mooney-Rivlin hyperelastic model following the method provided in [40, 41]. The shear moduli of the Tissue-1, Tissue-2, and Tissue-3 were identified as 2.05 ± 0.03, 1.51 ± 0.05, 0.54 ± 0.03 kPa, respectively.

Setup

For the validation tests, an RCI system with tendon-driven catheter was prototyped. The RCI system was comprised of mechanical, electrical and software modules. Fig.3.6(a) depicts the components of the modules. To drive the tendon upward and downward, two independent DC motors were used. The DC motors were equipped with built-in encoders and were controlled through a current controller interface (VINT Hub, Phidgets Inc., AB, Canada). Fig. 3.6 (b) summarizes the software structure which encompassed two main sub-modules: user interface (UI), and firmware (FW). The UI was the graphical user interface through which the desired current through each motor was set by the user and real-time image processing was performed.

Since in this study only one motor was used to bend the prototyped catheter, T_1 was considered in the analysis and T_2 was assumed as zero. As identified in Sec. 3.4.3, the tension in the tendon T_1 was proportional to the current draw of the DC motor I_m such that:

$$T_1 = \frac{2K_m}{D_p} I_m, \tag{27}$$

where, $K_m = 0.0169\ \frac{\text{mNm}}{\text{mA}}$, and $D_p = 20$mm.

During the test and for each frame, the shape of the catheter shaft was captured in using a USB camera (600×800 pixel resolution, model C920; Logitech, Lausanne, Switzerland) following the methodology described in Sec. 3.4.2.

Protocol

To evaluate the accuracy of the proposed method for force estimation, the catheter was bent from rest (straight shape) with three different speeds, i.e. slow, fast, manual. For bending tests, the current feed to Motor-1 was increased linearly from 0 to 0.9 A in time periods of 40s and 20s for slow and fast speeds, respectively. In addition, for manual speed, the user would increase the current

feed by increments of 0.05 A in each step. The time period between the steps was arbitrary. While the catheter was bending, the UI traced the shape of the catheter and extracted its tip position. Also, force estimation was performed based on the motor current and tip position feedbacks. Meanwhile, the ground-truth tip force on the tissue phantoms was recorded using an ATI Mini40 force sensor (Fig. 3.6. This test protocol was repeated for three times for each tissue phantom. Fig. 3.3 depicts the test setup used in this experiment.

Results

Table 3.1 summarizes the results of the force estimation in terms of maximum absolute error (MAE) and root-mean-square (RMS)-error (average of three repetitions) in the slow, fast and manual bending of the catheter. Since the catheter was not in contact with the tissue phantoms, there were zero force domains at the beginning of all the force-time curves. Once the tip of the catheter came into contact with the tissue phantoms, the estimated force increased due to increasing the indetation depth of the catheter tip into the tissue phantom. Afterwards, the contact force became steady as more current draw into the motor would not suffice to overcome the indentation resistance in the tissue phantoms. This phenomenon might be related to the nonlinear mechanical properties of the tissue phantoms whereas the tangent stiffness of the tissue phantoms increases nonlinearly (power-law, Mooney-Rivlin) with indentation depth. Nevertheless, the results showed that the system was fairly accurate in estimating the contact force in fast, slow, and manual velocities. The average RMS-error for all three polymeric tissue phantoms was in the range of [5.3,8.1]$\times 10^{-3}$ N. More specifically, the RMS-error was 6.5$\times 10^{-3}$ N, 5.2$\times 10^{-3}$ N and 8.2$\times 10^{-3}$ N for the slow, fast and manual movement of the catheter, respectively. Moreover, the computation time for force estimation was consistent across the tests, i.e, 0.0252s, 0.0280s and 0.0258s. Considering the fact that image acquisition frame-rate was 33 ± 5 the actual computation time for force estimation could be smaller than the estimated values. Another finding in this experiment was that the accuracy was higher in fast and slow speed compared to the manual input. The reason might be related to the observation that the settling time for the motor current was larger in manual test than the fast and slow tests. Nevertheless, the RMS-error of manual tests was below 0.01 N (5%) in all of the manual experiments. Furthermore, wilcoxon's signed rank test with confidence interval of 5% (p¡0.05) revealed

Table 3.1: Results of Study I on Polymeric Tissue Phantoms.

Phantom Tissue	Tendon rate	Max. F_{tip} (Estimated) (N)	Max. F_{tip} (Reference) (N)	Max. Abs. Error (N)	RMS Error (N)
Tissue-1	Slow	0.1909	0.1999	0.0397	0.0091
	Fast	0.1961	0.1831	0.0139	0.0080
	Manual	0.1143	0.1297	0.0181	0.0072
Tissue-2	Slow	0.1506	0.1545	0.0248	0.0056
	Fast	0.1485	0.1476	0.0052	0.0017
	Manual	0.1377	0.1480	0.0189	0.0087
Tissue-3	Slow	0.1654	0.1688	0.0160	0.0048
	Fast	0.1591	0.1606	0.0289	0.0058
	Manual	0.1045	0.1170	0.0176	0.0088

that the estimated accuracy metrics were not significantly different between the slow, fast, and manual tests. This finding showed that the performance of the proposed force estimation framework was not dependent on the tissue properties, thus does not necessitate real-time tissue characterization. Fig. 3.9 shows the correlation diagram of the estimated and ground-truth contact force. It was observed that except for the third run of fast test, the estimated force and ground-truth were in a semi-linear correlation. The correlation diagram of the manual test was not as linear as the slow and fast tests however it followed the same linear trend. Moreover, the linearity of the correlation diagram increased with contact force for the three test speeds.

3.5.2 Study II: *ex-vivo* Validation

Setup

To evaluate the performance of the developed method on real biological tissue, a series of fast, slow, and manual catheter bending similar to Validation Study-I was performed on a freshly excised porcine atrial tissue. To this end, the same RCI system as in Study-I was used. Fig.3.10 depicts the porcine cardiac tissue that was excised to expose the left atrial tissue. The excision was performed using a surgical blade (No. 10) and the tissue was fixated on a glass plate secured on the ATI Mini40

force sensor. During the tests, the ATI Mini40 sensor recorded the ground-truth reference values for contact force.

Protocol

A similar test protocol to Study-I was adopted for this experiment. The catheter was bent with three speeds, i.e., slow, fast, and manual. The test was repeated for three times for each speed.

Results

Table 3.2 summarizes the results of Study-II. The results showed that proposed method was accurate in estimating the contact force at the tip of the catheter. The RMS-error of the proposed method was 0.010 N ($\approx 5.5\%$), 0.009 N (5%), and 0.012 N ($\approx 6.5\%$), for slow, fast, and manual tests. In this set of experiments, it was observed that the slope of the rise in the contact force after initial contact was less that Study-I. The reason might be related to the softer mechanical properties of the biological tissue compared to the tissue phantoms. Also, it was observed that almost in none of the tests, the contact force reached the final plateau that indicated the ability of the RCI system to overcome the nonlinear indentation resistance of the porcine tissue. Another finding in Study-II was the increased time to the beginning of the rise in the contact force, for the first, second, and third re-tests. This observation might be related to the fact that since the cardiac tissue is highly viscoelastic, the effects of the first indentation was not completely vanished after each re-test. In other words, there was an initial indentation in the tissue in the contact area as a result of the previous catheter indentation. Nevertheless, as shown in Fig. 3.8, the estimated and ground-truth contact forces were in fair agreement. This observation confirms that not only the proposed method is independent from elastic properties of the tissue, but also is it not affected by the temporal history of previous indentations, e.g., caused by viscoelasticity. Another prominent finding of this study was that as depicted in Fig. 3.12 the estimated force and ground-truth were in a fairly linear correlation. Although, the correlation was initially nonlinear (for contact forces below 0.06N), it reaches a fairly linear pattern that considering the low error in estimation, shows that the acceptable performance of the proposed method.

Table 3.2: Results of Study II on porcine atrial tissue.

Tendon rate	Max. F_{tip} (Estimated) (N)	Max. F_{tip} (Reference) (N)	Max. Abs. Error (N)	RMS-Error (N)
Slow	0.1841	0.1770	0.0330	0.010
Fast	0.1909	0.1799	0.0260	0.009
Manual	0.1835	0.1766	0.0258	0.012

3.6 Conclusion

The objective of this study was to propose and validate a contact force estimation framework for tendon-driven soft ablation catheters. Considering the standard range of contact force during ablation procedures, i.e., 0.1–0.3 N, the proposed method showed an estimation error of less than 6.5% (of maximum force). The accuracy of the system was consistent among various tendon rates and with various mechanical properties of tissue phantoms and in the ex-vivo test. The proposed method exhibited higher estimation accuracy compared to Wahrburg *et al.* [162], Zhao *et al.* [163] and Khoshnam *et al.* [112] [113].

Another contribution of this study was that the proposed force estimation framework is purely mechanistic and proposes a semi-analytical solution to the force estimation problems as an inverse mechanical problem. This semi-analytical solution bypassed the need for iterative numerical solution and facilitated real-time computation. Also, the proposed methodology does not rely on small deformation assumption for the catheter which has been a theoretical limitation for some of the proposed methods in the literature. One of the limitations of this study was that the shape of the catheter was assumed to be of single radius arc. In practical scenarios, this assumption might be violated especially with more slender catheters. Also, the deformations considered in this study were single-planar, in practice, the catheter might experience bi-planar deformation that violated this assumption. Moreover, this work can be further extended to find a semi-analytical solution for a 3D multi-tendon driven catheter which would bend in 3D space and result in 3D contact force. Nevertheless, such a deformation requires adopting a 3D shape reconstruction methodology that could exacerbate the computational cost of the procedure for real-time applications.

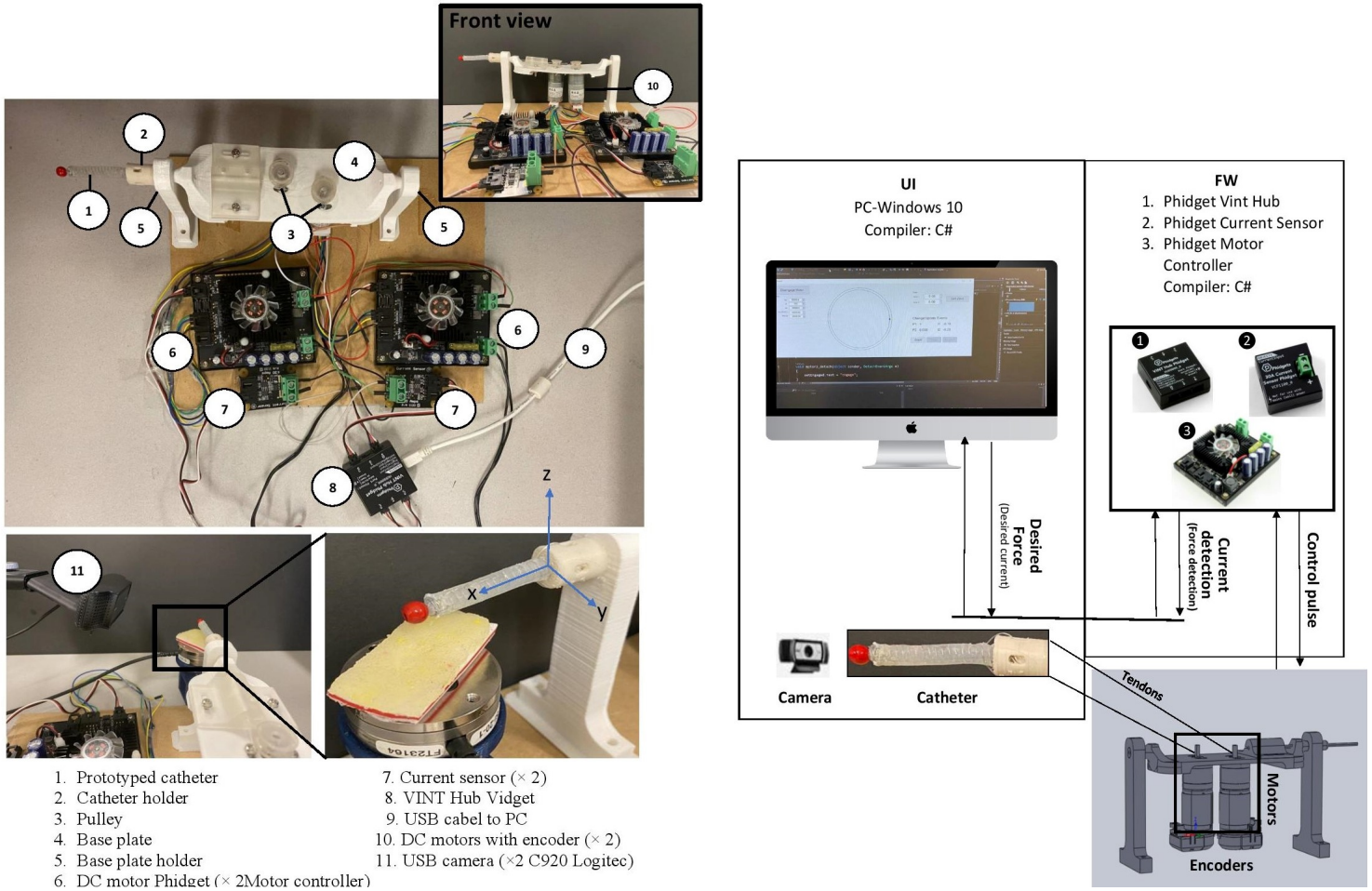

(a) (b)

Figure 3.6: (a) Components of the mechanical and electrical modules in the prototyped RCI device. (b) Software architecture of the UI and FW. FW, firmware; RCI, robotic catheter intervention; UI, user interface.

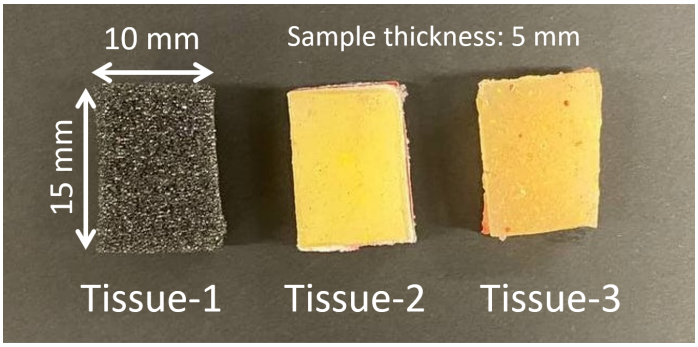

(a)

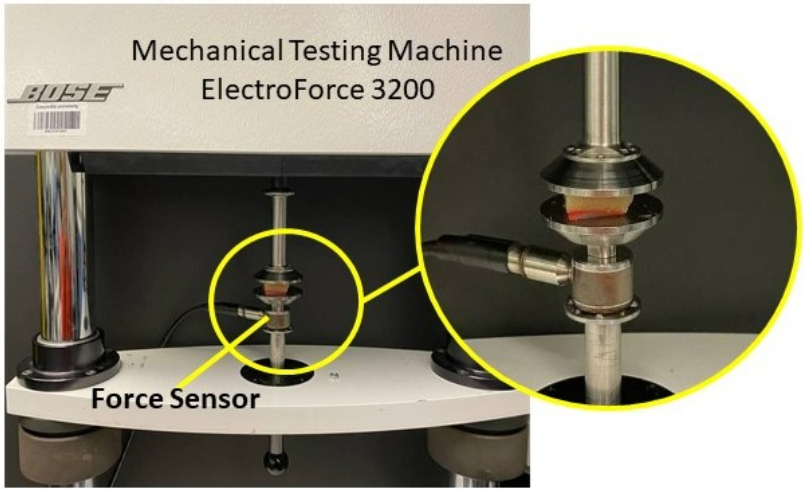

(b)

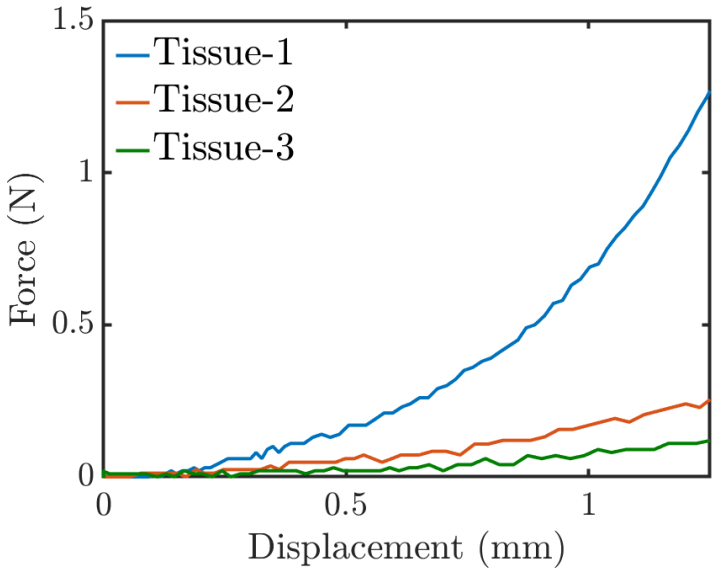

(c)

Figure 3.7: (a) Representative samples of Tissue-1, Tissue-2, and Tissue-3 with their nominal dimensions, (b) experimental setup for mechanical characterization of the tissue phantom samples, (c) force-displacement diagram of the tissue phantoms.

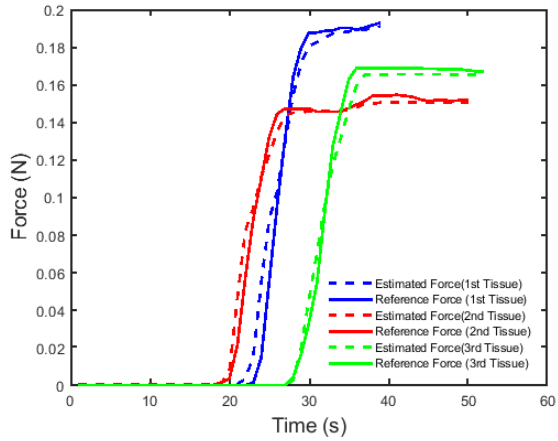

(a)

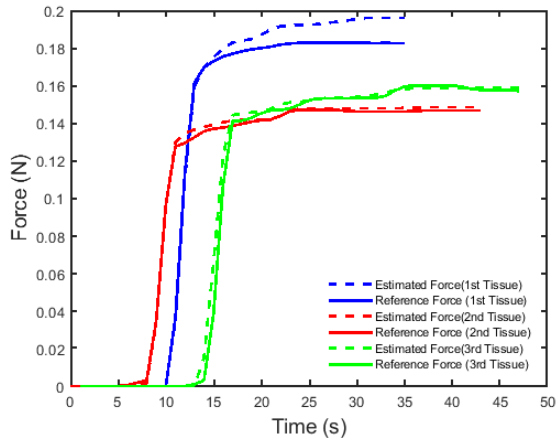

(b)

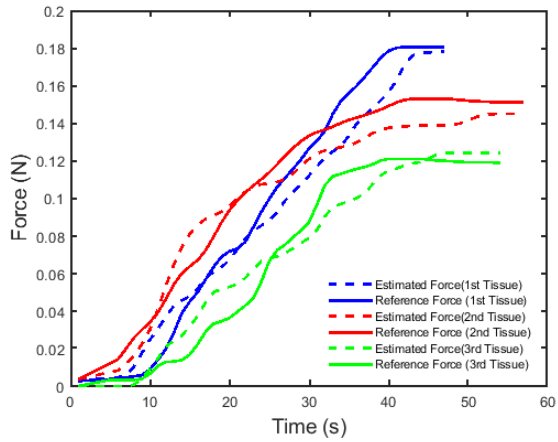

(c)

Figure 3.8: Comparison of the estimated tip force with ground-truth in Study I for different tendon rates (a) slow, (b) fast, (c) manual.

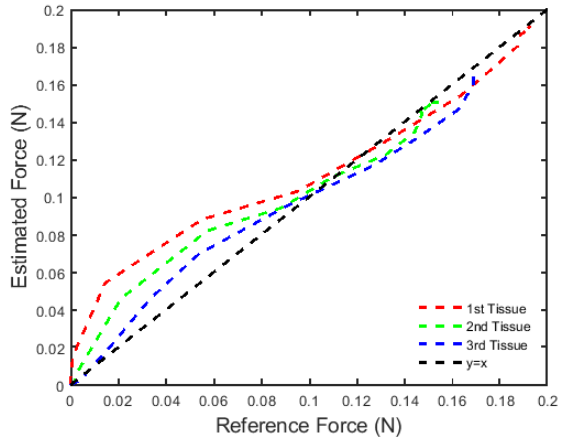

(a)

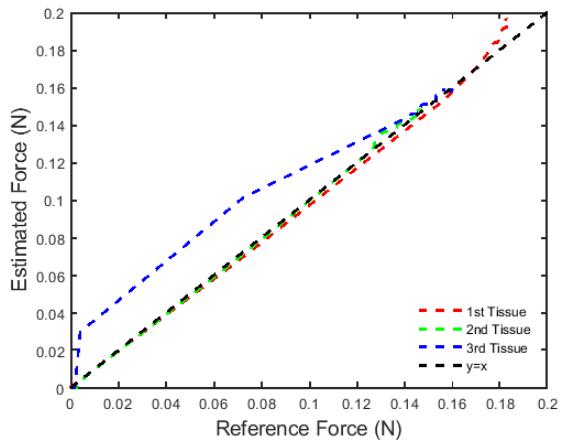

(b)

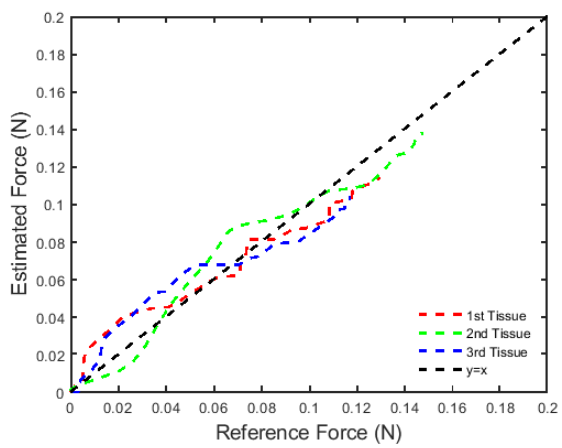

(c)

Figure 3.9: Correlation of the estimated tip force with ground-truth in Study I for different tendon rates (a) slow, (b) fast, (c) manual.

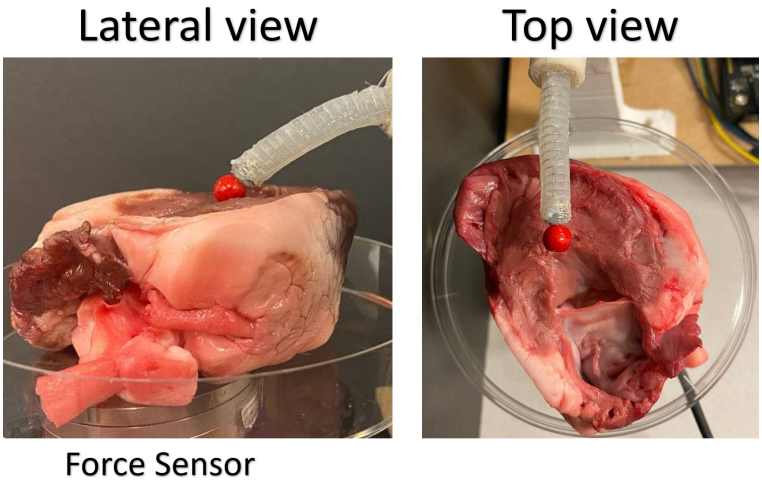

Figure 3.10: Tip of the catheter in contact with the porcine atrial tissue in Study II.

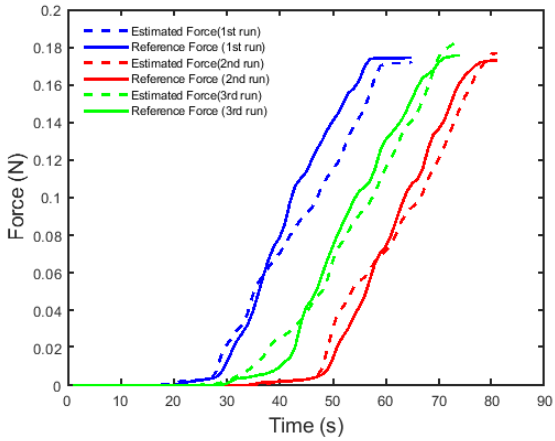

(a)

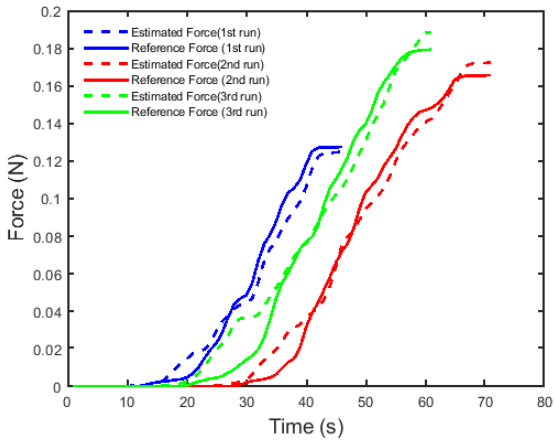

(b)

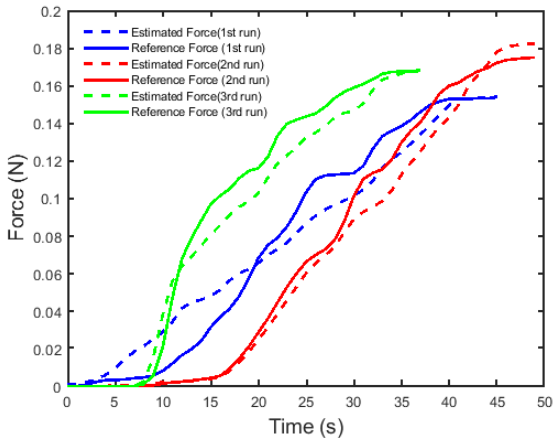

(c)

Figure 3.11: Comparison of the estimated tip force with ground-truth in Study II for different tendon rates (a) slow, (b) fast, (c) manual.

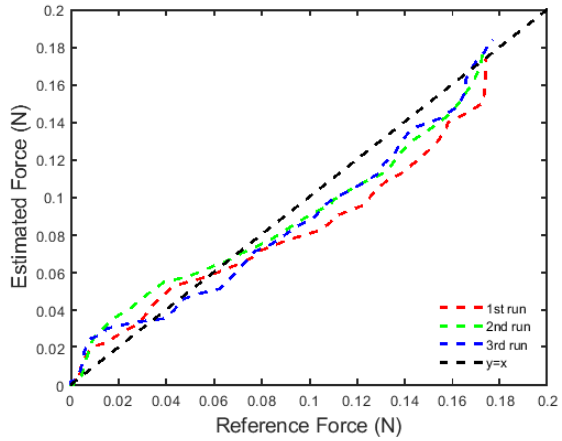

(a)

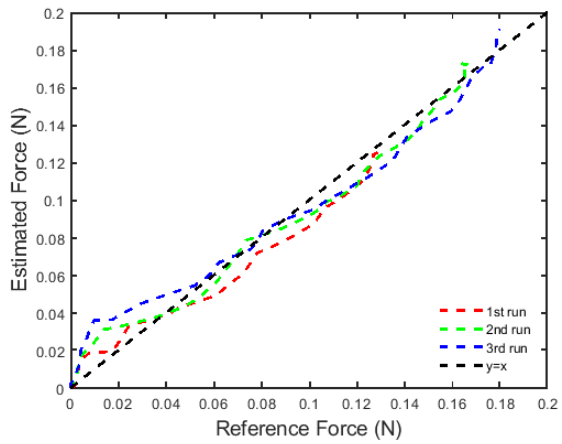

(b)

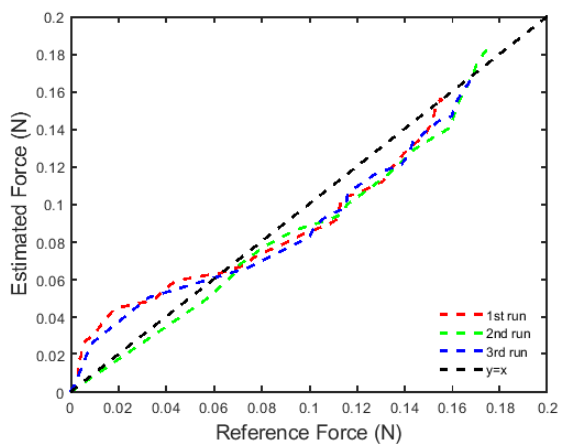

(c)

Figure 3.12: Correlation of the estimated tip force with ground-truth in Study II for different tendon rates (a) slow, (b) fast, (c) manual.

Chapter 4

Comparison of Mechanistic and Learning-based Tip Force Estimation on Tendon-driven Soft Robotic Catheters

4.1 Abstract

Researchers have adopted mechanistic and learning-based approaches for tip force estimation on soft robotic catheters. Typically the literature attributes the mechanistic methods with more accuracy while indicate the learning-based methods outpace in computational time. In this study, a previously validated mechanistic tip force estimation method was compared with four leaning-based methods, i.e. support-vector-regression (SVR), random-forest (RF), AdaBoost (Ada), and deep neural network (DNN). The learning-based methods were trained on experimental data acquired from a robotic catheter, developed in-house. The accuracy of force estimation using the five methods were compared with the ground truth forces in a teleoperated catheter manipulation test. Moreover, the capability of the learning-based models in contact detection, i.e., detection of the onset of tip contact, were compared with the ground truth. The results showed that the mechanical model had a mean-absolute error (MAE) of 8.8 mN while the MAE of SVR, RF, Ada, and DNN were 5.6, 5.2, 5.3, and 5.1 mN, respectively. Moreover, the accuracy and precision of the mechanistic model for

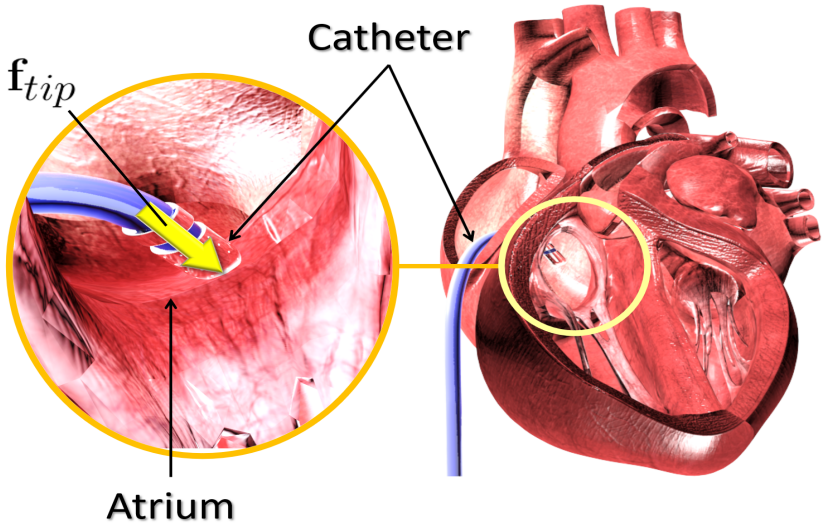

Figure 4.1: Schematic view of RFA catheter in contact with cardiac tissue.

contact detection was 89.2% and 91.7%, respectively, while these were 97.0%, 97.7%, 97.6%,and 97% and 97.9%, 98.3%, 97.8%, and 98.8% for the SVR, RF, Ada, and DNN, respectively. The comparison showed that with hyper-parameter optimization the learning-based models surpassed the mechanistic model in accuracy and precision, while both method approaches revealed acceptable performance for the proposed application.

4.2 Introduction

For radio-frequency ablation (RFA) therapy the success of the procedure highly depends on maintaining an optimal range of contact force between the RFA catheter tip and cardiac tissue (Fig. 4.1). The literature has reported the desired level of RFA contact force to be 0.1 ± 0.3 N with a minimum force-time (FTI) integration of 4 Ns [32, 164]. As such, tissue damage or vessel perforation in with excessive contact force, and ineffective ablation with insufficient contact force may occur [24].

During conventional RFA, surgeon rely on their tactile perception at the proximal end of the catheter that may be altered by patient's heart motion and friction between the catheter and vascular sheath. Moreover, the flexible nature of RFA catheters avoid preserving the favourable force

contact relying on proximal insertion. Steerable tendon-driven catheters have been widely used for their maneuverability inside the atrium [23,53]. The shape of the distal end of the steerable catheter is controlled through pulling a set of agonist-antagonist tendons [53]. Hence, such catheters, unless equipped with expensive sensors, cannot provide tip force information. In case of robot-assisted intervention, surgeons lose their subtle tactile perception as the intervention is performed through teleoperation.

For improving the accuracy of contact force estimation during robotic- based RFA, attempts have been made to develop sensor-embedded catheters as a means to provide surgeons with tactile feedback [165]. However, the compromised maneuverability of the catheter distal shaft due to added weigh, the high cost of sterilization of tools at high temperature and the disposable nature of catheters have hindered their wide adoption.

On the other hand, force estimation algorithms do not necessitate the use of sensing hardware at the tip of the catheters. The sensor-free force estimation algorithms typically utilize mechanistic or heuristic (learning-based) models for tip force estimation. Mechanistic approaches often simplify the catheter shape as a curve, in which piece-wise constant curvature (PCC) is the most common method [113, 126, 166]. These models involve simplification of the catheter shape or the external forces, friction, tendon slack, and material non-linearities which can affect estimation accuracy. Considering such non-linearities in mechanistic approach may result in model insufficiency and inaccuracy.

Alternatively, heuristic models such as machine learning and deep learning models have favorable results for real-time applications as they offer a low computational cost and the ability to capture the non-linearities [24]. In an early effort, Khoshnam *et al.* [112] proposed a Gaussian mixture model (GMM) to predict the contact force of conventional steerable catheters using distal shaft shape analysis. However, the accuracy was reported to be 80%. Rafii- Tari *et al.* [167] also developed the movement kinematics of catheter in robotic catheter intervention (RCI) system using GMM. In another effort GMM was used to model the catheter kinematics and kinematic control of catheters [168]. Despite the promising results of GMM in acquiring the non-linearities, it requires complex data preparation. Neural network (NN) as another heuristic approach is widely adopted. In an early effort, NN was utilized to compensate material non-linearities in proposing the kinematics

of continuum robots [169]. As a recent study, Jolaei *et al.* [144] proposed a learning- based (NN) inverse kinematics in conjunction with support vector machine method to control the tip position of a robotic tendon- driven catheter. Lastly, a merely data-driven method based on NN was suggested to estimate the force on da Vinci surgical robot using measurements from joint encoders and currents [170, 171].

4.2.1 Objective and Contributions

Reviewing the literature, there is a gap in direct comparison the performance of mechanistic versus learning-based methods for a similar dataset of experimental tip force data. Therefore, this study was aimed at comparing a previously validated mechanistic model [133] with four learning-based models trained on the same dataset for consistency.

The main contributions of this study were:

(1) Development of four learning-based tip force estimation (regression) models for tendon-driven soft catheters,

(2) Development of four learning-based contact detection (classification) models for tendon-driven soft catheters, and

(3) comparison of the performance of the developed learning-based models with a previously validated mechanistic model in terms of accuracy and precision in contact force estimation (regression) and contact detection (classification).

4.3 Material and Methods

In this section, first a summary of the mechanistic model for force estimation and contact detection models are provided. Afterwards, the detail of the four learning-based models, i.e., support-vector-regression (SVR), random forest (RF), AdaBoost (Ada), and deep neural network (DNN) are provided. Next, the experimental setup to acquire the training and test datasets and performance metrics are introduced.

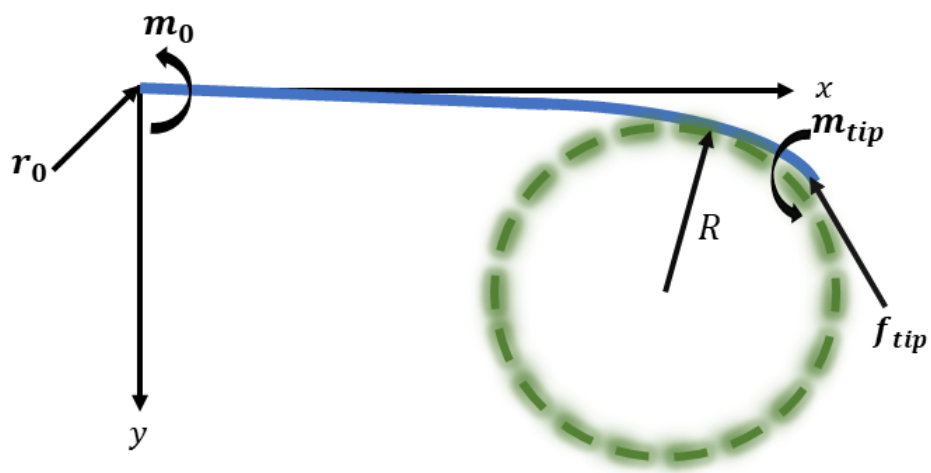

Figure 4.2: Free-body diagram of a deformed steerable catheter with contact force applied at its tip.

4.3.1 Mechanistic Method

Force Estimation–Regression

Fig.4.2 represents the free-body- diagram (FBD) of a steerable catheter in contact with the atrial tissue. As mentioned before, steerable RFA catheter are steered by a set of agonist- antagonist cables anchored to its tip, which result in tensile force at the tip of the catheter. $\mathbf{m}_{tip}$ and $\mathbf{f}_{tip}$ represent the force and moment at the tip of the catheter, respectively. Similarly, $\mathbf{m}_0$ and $\mathbf{r}_0$ are constant reaction force and moment at the base point of the catheter.

The catheter was modeled as a curved line object which also satisfied the Euler- Bernoulli beam assumption. The catheter was fabricated to have length of $40mm$ and a diameter of $3mm$ which replicates the 18-Fr clinical catheters [159]. The shape of the catheter was obtained real- time through using stero- camera which revealed the pasteurised continues function describing the shape of the catheter as $x = x(s)$ and $y = y(s)$ (s is an independent parameter $s \in [0, 1]$), where $s = 0$ and $s = 1$ correspond to the base and tip of the catheter, respectively. By assuming tendon forces at the tip of the catheter $\mathbf{T}_1$ and $\mathbf{T}_2$ as a-priori knowledge, obtained from control system, the static equilibrium equation of the catheter in combination with Euller- Bernoulli beam theory can be solved. Hence, force estimation problem is defined as a minimization equation to find tip force ($\mathbf{f}_x$,$\mathbf{f}_y$) that minimizes the residual absolute error Γ:

$$\text{minimize} \quad \Gamma = |m_z(s) - \frac{EI}{R(s)}|, \tag{28}$$

Where $\mathbf{m}_z(s)$ is the moment with respect to z axis, at each arbitrary point (s) along the catheter curvature and EI is the flexural rigidity of the beam. For numerical solution of the Eq.28, two scenarios can be assumed. Firstly, the catheter moves in free space ($\mathbf{f}_x = \mathbf{f}_y = 0$), in this case the residual function turns to be constant and the minimization problem discloses zero contact forces . Secondly, the catheter tip touches the tissue surface, in this scenario the catheter length can be discretized in 9 sections, thus the Eq. 28 can be reordered as:

$$\mathbf{A} \begin{pmatrix} f_x \\ f_y \end{pmatrix} - \mathbf{b} = 0, \tag{29}$$

where,

$$\mathbf{A} = \begin{pmatrix} x(1) - x(0) & y(0) - y(1) \\ \vdots & \vdots \\ x(1) - x(0.9) & y(0.9) - y(1) \end{pmatrix}, \mathbf{b} = - \begin{pmatrix} \delta(T_1 - T_2) - \frac{EI}{R(0)} \\ \vdots \\ \delta(T_1 - T_2) - \frac{EI}{R(0.9)} \end{pmatrix}. \tag{30}$$

The matrix A components relies on curvature extraction at each specific point along catheter distal shaft using image processing technique. Besides, vector B builds upon tension forces obtain from motor signals and unique curvatures of the catheter along its length.

Using mechanical properties of the steerable catheters, the inverse solution reveals the external force at the tip of the catheter $\mathbf{f}_x$ and $\mathbf{f}_y$. Details of the mechanical model derivation and image-based force estimation technique can be found in [133].

Contact Detection–Binary Classification

The contact detection on the mechanistic model was performed with *a-priori* information of the force estimation. To this end, the tip of the catheter was considered in contact if the estimated force from the regression model was zero. Zero-force condition was defined if the estimated force

was less than the 1 mN. Thus, in fact the contact detection was serialized with the force estimation and could not be separated. In contrast and as will be explained, the contact detection could be parallelized with force estimation using the learning-based methods as they utilized two separate models for contact detection (classification) and force estimation (regression).

4.3.2 Learning-based Methods

Input Features

Based on the literature, e.g., [126, 133], the tip contact force of the soft tendon-driven catheters can be estimated using the electric current draw of the driver motor (I), rate of change of the current ($\dot{I}$), tendon length (L), and tendon velocity ($\dot{L}$). Therefore, the feature vector $\mathbf{X}$ used as the input to the learning-based models was:

$$\mathbf{X} = (I, \dot{I}, L, \dot{L}). \tag{31}$$

Output–Force estimation

The output of the models, y for force estimation was the total tip force on the catheter. The total forces were obtained from the experiment and were calculated as the norm of the tip force vector (obtained from an ATI Mini40 force sensor in the experimental setup):

$$y = ||\mathbf{f}_{tip}|| = \sqrt{f_{x_{tip}}^2 + f_{y_{tip}}^2 + f_{z_{tip}}^2}, \tag{32}$$

where, $f_{x_{tip}}$, $f_{y_{tip}}$, and $f_{z_{tip}}$ were the Cartesian components of the tip force directly measured by the ATI force sensor.

Output–Contact Detection

For contact detection the dataset was labeled with binary labels as follows:

$$\text{Contact State} : \begin{cases} y = 0, & ||\mathbf{f}_{tip}|| \leq 1\text{mN} \\ y = 1, & \text{otherwise} \end{cases}, \tag{33}$$

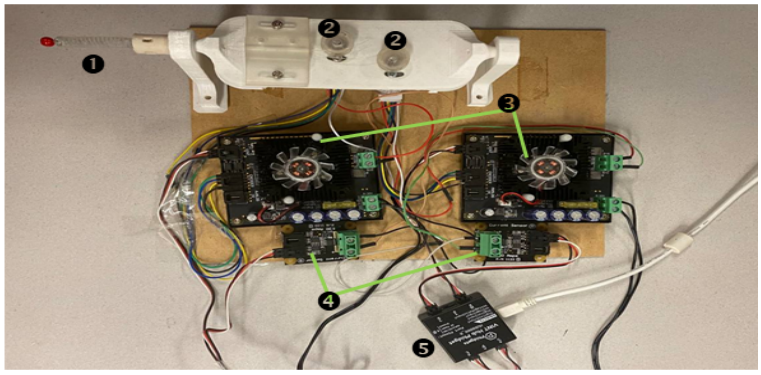

1. Prototyped catheter
2. Pulleys
3. DC motor Phidget (X2 Motor controller)
4. Current sensor (X2)
5. VINT Hub Phidget

(a)

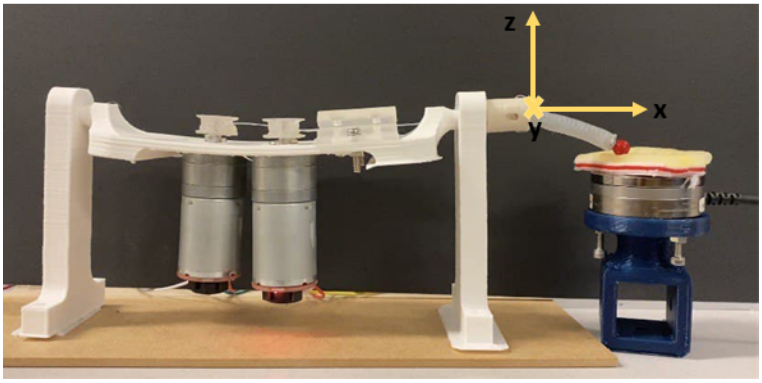

(b)

Figure 4.3: (a) Components of the developed RCI system (b) Catheter deflection during interaction with phantom tissue

where '0' and '1' labels corresponded to 'non-contact' and 'in-contact' status.

Dataset

The models were trained on experimental dataset obtained from the in-house robot-assisted cardiovascular intervention system depicted in Fig. 4.3.

As shown, data was collected in both non-contact and in-contact conditions. The RCI system was teleoperated by controlling the catheter movement and smoothly interacting with tissue phantom with arbitrary intervals. Imitating the realistic catheter movement in surgery, varying velocities were applied to include various contact forces. The experiment was designed to have a balanced mix of non-contact (catheter movement in free space) and in-contact (catheter interaction with tissue

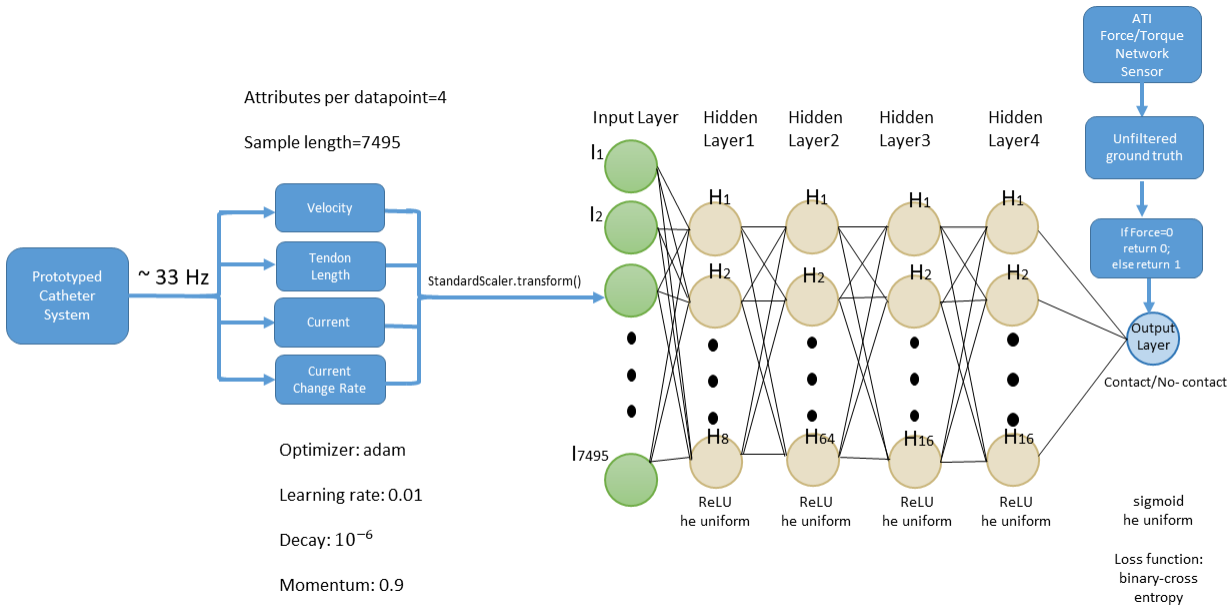

Figure 4.4: Network structure neural network architecture for estimation the contact vs. non-contact status of the catheter

phantom). Simultaneously, the input features were recorded and obtained through a dedicated in-house control software framework (C#).

The RCI sampling rate was set to be 33 Hz, and it was synchronised with ATI Mini40 sensor. Current I and its rate of change $\dot{I}$ were obtained from current sensors, and velocity was estimated from the motor encoder. Moreover, the length of tendon that was actuated was estimated as:

$$L = r_p \theta \tag{34}$$

where, θ was the motor shaft's rotational position in radians, and $r_p = 10$mm, was the pulley's radius. The RCI system was teleoperated by controlling the catheter movement and smoothly interacting with tissue phantom with arbitrary intervals. Imitating the realistic catheter movement in surgery, varying velocities were applied to include various contact forces. The experiment was designed to have a balanced mix of non-contact (catheter movement in free space) and in-contact (catheter interaction with tissue phantom). Simultaneously, the input features were recorded and obtained through a dedicated in-house control software framework (C#).

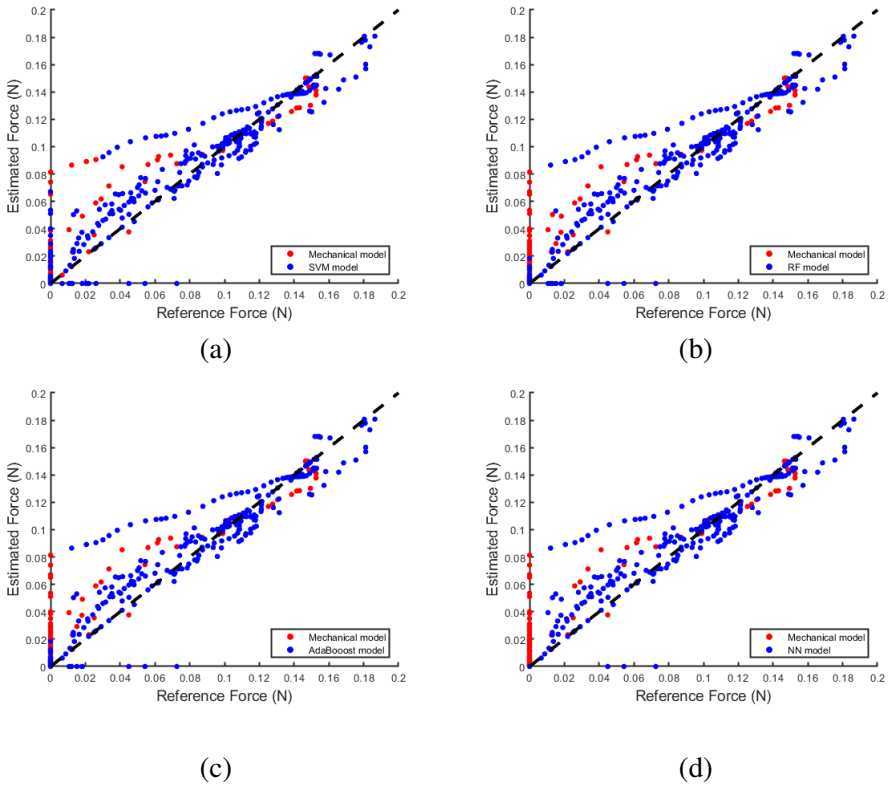

Figure 4.5: Model evaluation results. The results are generated from catheter movement in free space and during palpation with varying intervals and intensities

The RCI sampling rate was set to be 33 Hz, and it was synchronised with ATI Mini40 sensor. Current I and its rate of change $\dot{I}$ were obtained from current sensors, and velocity was estimated from the motor encoder. Moreover, the length of tendon that was actuated was estimated as:

$$L = r_p \theta \tag{35}$$

where, θ was the motor shaft's rotational position in radians, and $r_p = 10$mm, was the pulley's radius. The training and testing set have a standard ratio of 80 to 20. The validation set is not trained on, but in NN is used after every epoch during training to minimize over-fitting.

Model Architectures

The details of the developed learning-based models are provided in Table 4.2. The hyper-parameters of the utilized ensemble methods, i.e., RF and AdaBoost, were tuned by randomised

Table 4.1: Performance of the models for tip force estimation (regression).

Model	MAE (mN)	RMSE (mN)
Mechanical	8.8	15.7
SVM	5.6	12.1
RF	5.2	11.8
AdaBoost	5.3	11.9
NN	5.1	11.8

hyper-parameter search using Scikit-learn library in Python. Keras library was utilized to implement a fully-connected feedforward neural network, with Tensorflow as the backend [172]. The DNN structure was selected manually, starting from a single perception. The best performance was observed with 4 hidden layers and with 8, 64, 16, and 16 neurons in the first to the fourth layer, respectively. Fig.4.4 shows the complete data flow of the neural network. ReLU activation function was utilized as the intermediate activation function in network structure. The output layer uses the sigmoid activation function, and the weigh initializer was set to be He uniform initializer. Additionally, the optimization algorithm was Adaptive Moment Estimation (Adam) and the loss function was binary cross-entropy. The learning parameters were set as learning rate of 0.01, decay of $1e-6$, and momentum of 0.9.

A total of 7495 samples were recorded in the dataset with four components in each vector (7495×4). The output dimension was 1. Each model was once trained as a regressor for force estimation and once as a classifier for contact detection.

4.4 Results and Discussion

Fig. 4.5 shows the correlation between the estimated forces and ground-truth with one-to-one comparison of the mechanistic model with learning-based models.

Table. 4.1 summarizes the evaluation results on the test dataset. It was observed that the learning models decreased the errors in comparison with the mechanistic model. The deviation of the mechanical model results from ground-truth at small forces, i.e., 'non-contact is relatively higher than

Table 4.2: Hyper-parameters of the learning-based models.

Models	Hyper-parameters		
	Search-space	Selected	Accuracy
SVM	{'C': [0.1, 1, 10, 100, 1000], 'gamma': [1, 0.1, 0.01, 0.001, 0.0001], 'kernel': ['rbf','linear', 'sigmoid']}	{'kernel': 'rbf', 'gamma': 0.0001 'C': 100}	96%
RF	{'n_estimator': [200, 400, 600, 800, 1000, 1200, 1400, 1600, 1800, 2000], 'max_depth':[10, 20, 30, 40, 50, 60, 70, 80, 90, 100, 110] 'max_features': ['auto', 'sqrt']}	{'n_estimators': 200, 'max_features': 'sqrt', 'max_depth': 90}	98%
AdaBoost	{'n_estimators' : [20,50,80,110, 140,170,200] 'algorithm' :['SAMME', 'SAMME.R']}	{'n_estimators': 170, 'algorithm': 'SAMME'}	98%
DNN	{No. hidden layers: [1,4,8,12] batch size:[25,50,100] Optimization algorithm:[SGD, Adam, RMSProp]}	{No. hidden layers: 4 batch size:25 Optimization algorith,: SGD} layer structure:[8,64,16,16,1]	97%

'in-contact' points. However in contrast to the mechanical model, the learning models could accurately capture the non-contact status that can be used to rule-out non-accurate force estimations. As provided in Table 4.2, the accuracy of all used learning models are relatively high and SVM, RF, AdaBoost and DNN can reduce the MAE by 32%, 36%, 35% and 37% compared to the mechanistic model, respectively. A notable finding was that both the mechanistic model and learning-based models were adequately accurate for the proposed application, as the acceptable range of mean-absolute-error for RFA applications is 10 mN [24]. Since the accuracy was not the best parameter to evaluate the performance of the learning models, the confusion matrix of learning algorithms are used to compare their feasibility (Fig. 4.6). As mentioned previously, the learning models can fill the gap for 0 N contact force detection where the catheter are not in contact with tissue phantoms, on the other hand as depicted in Fig. 4.5 the learning models do not show any anomalies in forces larger than 0.1 N where the sensitivity of force range becomes more significant. Thus, according to the catheter application and the necessity of the subtle tip force range, the number of false negative predictions can be a reliable parameter to evaluate the learning models performance. According to confusion matrix depicted in Fig. 4.6, DNN model with the least false negative could be a choice to be used in RCI systems.

Table 4.3: Performance of the models for contact detection (classification)

	Models				
	Mechanistic	SVM	RF	Ada	DNN
Accuracy (%)	89.2	97.0	97.7	97.6	97.0
Precision (%)	91.7	97.9	98.3	97.8	98.8

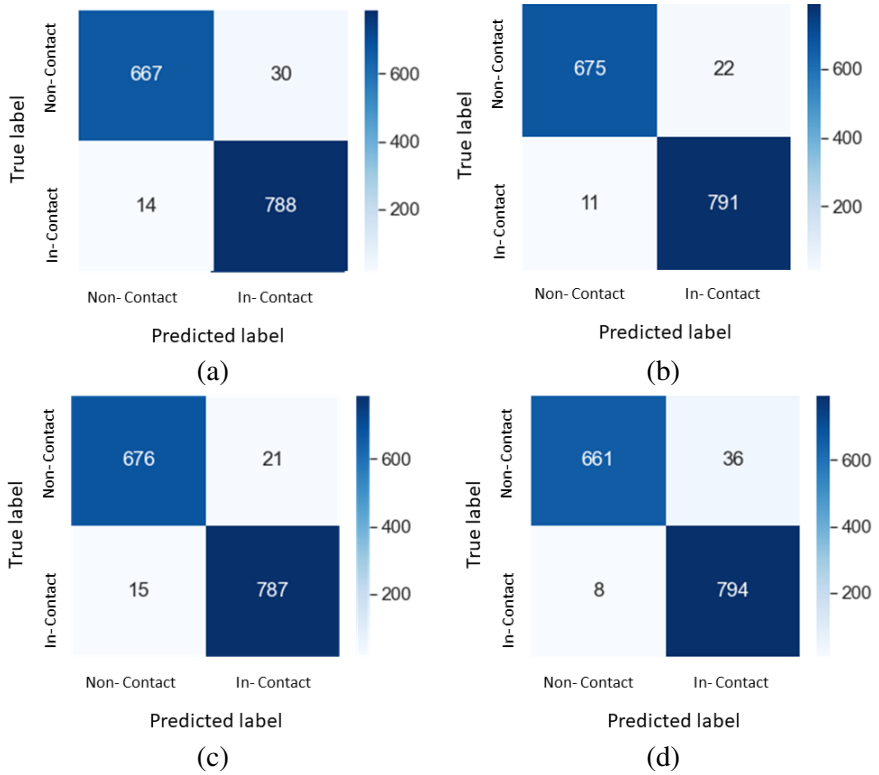

Figure 4.6: Comparison of confusion matrices of learning-based models for contact detection: (a) SVM (b) RF (c) AdaBoost (d) DNN.

For the contact detection, the accuracy and precision of the mechanistic model and learning-based methods were calculated based on the confusion matrices using Eq. 36.

$$\text{Accuracy} = \frac{\text{TP+TN}}{\text{TP+FP+FN+TN}}, \text{Precision} = \frac{\text{TP}}{\text{TP+FP}}, \tag{36}$$

where, TP, TN, FP, and FN indicate the true-positive, true-negative, false-positive, and false-negative values in the confusion matrices. Table 4.3 summarize the results of classification metrics. It was observed that while the minimum accuracy and precision for the learning-based methods was 97.0%

(SVM and DNN) and 97.8% (Ada), respectively, the mechanistic model's accuracy and precision were 89.2% and 91.7%. This clearly showed the superiority of the learning-based classifiers for contact detection. The reason might be related to the fact that binary contact classification with mechanistic model was simply an if-statement logic and it relied on the result of the force estimation might suffers from model insufficiency (due to model simplifications). Overall, the results show that the learning models are capable of predicting the tip force of the catheter without sensors at test time. Through using different phantoms with different stiffness in study, it was shown that the learning models have the potential to be generalized to new tissue phantoms on which they had not been trained.

By using learning models, a predictive model which is robust to variations and minimizes backlashes, hysteresis and complexity resulting from mechanical model has been developed.

Although the proposed method has demonstrated viability for providing tip force feedback, an unresolved problem is how to implement the proposed RCI in practice. Placing the force sensor to provide the ground truth within the patients body for retraining the learning models would be a challenge. One approach can be to investigate whether the dynamics of the catheter can be tuned during only free- space movement (non-contact status) of the catheter.

4.5 Conclusion

The proposed method demonstrated that mechanical model in conjunction with learning- based models can provide accurate force estimation in both non-contact and in-contact status of the catheter with respect to phantom tissues. Future work can further evaluate the performance of the proposed method, such as testing on different catheters of the same type to see the effect of different tear and wear on accuracy. Furthermore, the current method could be expanded to force estimation in 3D work-space for catheter movement. Performing an online learning to adopt learning models with new phantom as the catheter is palpating the tissue will enable the streamlining of learning process. This approach could be the first step in implementing the sensor-less force estimation for robotic based catheter systems.

Chapter 5

Conclusion and Future Works

5.1 Conclusions

In this thesis, a real-time image-based method for real-time steerable RFA catheter contact force estimation was developed and introduced in chapter 2. In this regard, a planar mechanical model of the RFA catheters with an unknown tip force (either in contact with endocardium tissue or moving in free space) was postulated. The inverse solution schema based on the catheter curvature was presented, and the results were verified with finite element solutions. The results were in compliance with the acceptable accuracy and real-time applications required for robot-assisted cardiac ablation procedures.

Next, an in-house steerable flexible tendon-driven catheter and a robotic catheter intervention system were designed and developed. Afterwards, firstly, a parameterized shape sensing method was proposed and used to interpolate the deformed shape of the catheter in real-time. Secondly, a mechanistic model of the catheter-based on large deformation was proposed. The proposed method was tested on three different polymeric tissue phantoms as well as porcine atrial tissue. Considering the favorable range of contact force during RFA (0.1 N -0.3 N), the system successfully predict the tip-tissue contact force.

Noteworthy, all the models developed in the RCI system were in-house which readily allows for maximal software-hardware integration.

5.2 Future Studies

To the best of the author knowledge, this work was the first to propose a real- time force estimation schema for the tendon-driven RFA catheters merely relying on catheter characteristics. Therefore the author acknowledges its limitations in assumptions and implementations. A summary of the propositions for the future work to address the limitations are as follows:

i. For future studies, an extension of this work could be dynamic modeling of the catheter and further extension of the planar model to the 3D simulation.

ii. Another improvement of this work would be adding a linear degree of freedom to the base of the catheter, or adding another DC motor to the rotate the whole system spatially. Such extensions would expand the feasible space of the catheter, however, increases the degrees of freedom and possibly alters the kinematics of the catheter.

iii. Another improvement would be to investigate the feasibility of the tip-tissue contact force by impedance control through using the results of the current research.

iv. Another improvement could be updating the kinematics of the catheter with multi- curvature assumption rather the single- curvature. Even though it will increase the complexity but may result in ,ore accurate results.

v. For another extension of this work, the force estimation method could be merely processed through the data obtained from the developed RCI system and the learning algorithms, e.g. ANN .

Appendix A

My Appendix

Appendix figure example is shown in A.1 below

Figure A.1: An figure example in Appendix A.

Bibliography

[1] M. Jolaei, A. Hooshiar, and J. Dargahi, "Displacement-based model for estimation of contact force between rfa catheter and atrial tissue with ex-vivo validation," in *2019 IEEE International Symposium on Robotic and Sensors Environments (ROSE)*. IEEE, 2019, pp. 1–7.

[2] W. G. Members, V. L. Roger, A. S. Go, D. M. Lloyd-Jones, E. J. Benjamin, J. D. Berry, W. B. Borden, D. M. Bravata, S. Dai, E. S. Ford *et al.*, "Heart disease and stroke statistics—2012 update: a report from the american heart association," *Circulation*, vol. 125, no. 1, pp. e2–e220, 2012.

[3] A. G. Kléber and Y. Rudy, "Basic mechanisms of cardiac impulse propagation and associated arrhythmias," *Physiological reviews*, 2004.

[4] L. J. Motloch and F. G. Akar, "Gene therapy to restore electrophysiological function in heart failure," *Expert opinion on biological therapy*, vol. 15, no. 6, pp. 803–817, 2015.

[5] P. J. Podrid and R. J. Myerburg, "Epidemiology and stratification of risk for sudden cardiac death," *Clinical Cardiology: An International Indexed and Peer-Reviewed Journal for Advances in the Treatment of Cardiovascular Disease*, vol. 28, no. S1, pp. 3–11, 2005.

[6] S. Stewart, C. L. Hart, D. J. Hole, and J. J. McMurray, "A population-based study of the long-term risks associated with atrial fibrillation: 20-year follow-up of the renfrew/paisley study," *The American journal of medicine*, vol. 113, no. 5, pp. 359–364, 2002.

[7] S. Colilla, A. Crow, W. Petkun, D. E. Singer, T. Simon, and X. Liu, "Estimates of current and future incidence and prevalence of atrial fibrillation in the us adult population," *The American journal of cardiology*, vol. 112, no. 8, pp. 1142–1147, 2013.

[8] X.-S. Wu, W. Cai, P. Zhu, and W. Yuan, "New strategies for arrhythmia treatment," *Journal of Cardiology and Therapy*, vol. 5, no. 1, pp. 756–763, 2018.

[9] T. E. o. E. Britannica, "heart," 2021, accessed = 2021-09-28. [Online]. Available: https://www.britannica.com/science/heart

[10] M. Mona, "Types of atrial fibrillation disease with causes & nursing intervention," 2015, accessed = 2015-06-23. [Online]. Available: http://nursingexercise.com/atrial-fibrillation-diease-causes-symptoms/

[11] D.-g. Fu, "Cardiac arrhythmias: diagnosis, symptoms, and treatments," *Cell biochemistry and biophysics*, vol. 73, no. 2, pp. 291–296, 2015.

[12] A. AlTurki, R. Proietti, V. Russo, T. Dhanjal, P. Banerjee, and V. Essebag, "Anti-arrhythmic drug therapy in implantable cardioverter-defibrillator recipients," *Pharmacological research*, vol. 143, pp. 133–142, 2019.

[13] P. Jaïs, R. Weerasooriya, D. C. Shah, M. Hocini, L. Macle, K.-J. Choi, C. Scavee, M. Haïssaguerre, and J. Clémenty, "Ablation therapy for atrial fibrillation (af) past, present and future," *Cardiovascular research*, vol. 54, no. 2, pp. 337–346, 2002.

[14] A. H. Hachem, J. E. Marine, H. A. Tahboub, S. Kamdar, S. Kanjwal, R. Soni, and K. Kanjwal, "Radiofrequency ablation versus cryoablation in the treatment of paroxysmal atrial fibrillation: a meta-analysis," *Cardiology research and practice*, vol. 2018, 2018.

[15] I. D. McRury and D. E. Haines, "Ablation for the treatment of arrhythmias," *Proceedings of the IEEE*, vol. 84, no. 3, pp. 404–416, 1996.

[16] R. A. Winkle, S. Mohanty, R. A. Patrawala, R. H. Mead, M. H. Kong, G. Engel, J. Salcedo, C. G. Trivedi, C. Gianni, P. Jais *et al.*, "Low complication rates using high power (45–50 w) for short duration for atrial fibrillation ablations," *Heart Rhythm*, vol. 16, no. 2, pp. 165–169, 2019.

[17] B. Hall, V. Jeevanantham, R. Simon, J. Filippone, G. Vorobiof, and J. Daubert, "Variation in left atrial transmural wall thickness at sites commonly targeted for ablation of atrial fibrillation," *Journal of Interventional Cardiac Electrophysiology*, vol. 17, no. 2, pp. 127–132, 2006.

[18] A. Bhaskaran, W. Chik, J. Pouliopoulos, C. Nalliah, P. Qian, T. Barry, F. Nadri, R. Samanta, Y. Tran, S. Thomas *et al.*, "Five seconds of 50–60 w radio frequency atrial ablations were transmural and safe: an in vitro mechanistic assessment and force-controlled in vivo validation," *EP Europace*, vol. 19, no. 5, pp. 874–880, 2017.

[19] J. Joseph and K. Rajappan, "Radiofrequency ablation of cardiac arrhythmias: past, present and future," *QJM: An International Journal of Medicine*, vol. 105, no. 4, pp. 303–314, 2012.

[20] S. Nath, J. P. DiMARCO, and D. E. Haines, "Basic aspects of radiofrequency catheter ablation," *Journal of cardiovascular electrophysiology*, vol. 5, no. 10, pp. 863–876, 1994.

[21] X. Hu, A. Chen, Y. Luo, C. Zhang, and E. Zhang, "Steerable catheters for minimally invasive surgery: a review and future directions," *Computer Assisted Surgery*, vol. 23, no. 1, pp. 21–41, 2018.

[22] R. U. M. center, "Robotic-assisted cardiac surgery." 2016, accessed = 2016-09. [Online]. Available: http://www.urmc.rochester.edu/encyclopedia/

[23] H. Rafii-Tari, C. J. Payne, and G.-Z. Yang, "Current and emerging robot-assisted endovascular catheterization technologies: a review," *Annals of biomedical engineering*, vol. 42, no. 4, pp. 697–715, 2014.

[24] A. Hooshiar, S. Najarian, and J. Dargahi, "Haptic telerobotic cardiovascular intervention: a review of approaches, methods, and future perspectives," *IEEE Reviews in Biomedical Engineering*, 2019.

[25] N. R. Smilowitz, J. W. Moses, F. A. Sosa, B. Lerman, Y. Qureshi, K. E. Dalton, L. T. Privitera, D. Canone-Weber, V. Singh, M. B. Leon *et al.*, "Robotic-enhanced pci compared to the traditional manual approach," *J Invasive Cardiol*, vol. 26, no. 7, pp. 318–321, 2014.

[26] A. Hooshiar, N. M. Bandari, and J. Dargahi, "Image-based estimation of contact forces on catheters for robot-assisted cardiovascular intervention," in *Proc. Hamlyn Symp. Med. Robot.*, 2018, pp. 119–120.

[27] G. Weisz, D. C. Metzger, R. P. Caputo, J. A. Delgado, J. J. Marshall, G. W. Vetrovec, M. Reisman, R. Waksman, J. F. Granada, V. Novack *et al.*, "Safety and feasibility of robotic percutaneous coronary intervention: Precise (percutaneous robotically-enhanced coronary intervention) study," *Journal of the American College of Cardiology*, vol. 61, no. 15, pp. 1596–1600, 2013.

[28] H. Rafii-Tari, C. J. Payne, C. Bicknell, K.-W. Kwok, N. J. Cheshire, C. Riga, and G.-Z. Yang, "Objective assessment of endovascular navigation skills with force sensing," *Annals of biomedical engineering*, vol. 45, no. 5, pp. 1315–1327, 2017.

[29] S. K. Neequaye, R. Aggarwal, I. Van Herzeele, A. Darzi, and N. J. Cheshire, "Endovascular skills training and assessment," *Journal of vascular surgery*, vol. 46, no. 5, pp. 1055–1064, 2007.

[30] R. Madder, P. Campbell, E. Mahmud, D. Wohns, T. Stys, R. Caputo, M. Leimbach, M. Parikh, V. Kasi, and G. Weisz, "Multi-center post-market registry for the evaluation of robotic assisted pci," *Journal of the American College of Cardiology*, vol. 67, no. 13S, pp. 224–224, 2016.

[31] M. E. Jacoby, M. Veerasamy, and R. D. Madder, "Robotic percutaneous coronary intervention," in *Textbook of Catheter-Based Cardiovascular Interventions*. Springer, 2018, pp. 133–143.

[32] D. C. Shah, H. Lambert, H. Nakagawa, A. Langenkamp, N. Aeby, and G. Leo, "Area under the real-time contact force curve (force–time integral) predicts radiofrequency lesion size in an in vitro contractile model," *Journal of cardiovascular electrophysiology*, vol. 21, no. 9, pp. 1038–1043, 2010.

[33] Y. Okumura, S. B. Johnson, T. J. Bunch, B. D. Henz, C. J. O'BRIEN, and D. L. Packer, "A systematical analysis of in vivo contact forces on virtual catheter tip/tissue surface contact during cardiac mapping and intervention," *Journal of cardiovascular electrophysiology*, vol. 19, no. 6, pp. 632–640, 2008.

[34] L. Di Biase, A. Natale, C. Barrett, C. Tan, C. S. Elayi, C. K. Ching, P. Wang, A. AL-AHMAD, M. Arruda, J. D. Burkhardt *et al.*, "Relationship between catheter forces, lesion characteristics,"popping," and char formation: experience with robotic navigation system," *Journal of cardiovascular electrophysiology*, vol. 20, no. 4, pp. 436–440, 2009.

[35] K. A. Hausegger, P. Schedlbauer, H. A. Deutschmann, and K. Tiesenhausen, "Complications in endoluminal repair of abdominal aortic aneurysms," *European journal of radiology*, vol. 39, no. 1, pp. 22–33, 2001.

[36] T. Kaneko and W. R. Chitwood Jr, "Current readings: Status of robotic cardiac surgery," in *Seminars in thoracic and cardiovascular surgery*, vol. 25, no. 2. Elsevier, 2013, pp. 165–170.

[37] N. Bandari, J. Dargahi, and M. Packirisamy, "Tactile sensors for minimally invasive surgery: a review of the state-of-the-art, applications, and perspectives," *IEEE Access*, 2019.

[38] N. M. Bandari, A. Hooshair, M. Packirisamy, and J. Dargahi, "Optical fiber array sensor for lateral and circumferential force measurement suitable for minimally invasive surgery: Design, modeling and analysis," in *Specialty Optical Fibers*. Optical Society of America, 2016, pp. JTu4A–44.

[39] T. Li, C. Shi, and H. Ren, "Three-dimensional catheter distal force sensing for cardiac ablation based on fiber bragg grating," *IEEE/ASME Transactions on Mechatronics*, vol. 23, no. 5, pp. 2316–2327, 2018.

[40] N. M. Bandari, R. Ahmadi, A. Hooshiar, J. Dargahi, and M. Packirisamy, "Hybrid piezoresistive-optical tactile sensor for simultaneous measurement of tissue stiffness and detection of tissue discontinuity in robot-assisted minimally invasive surgery," *Journal of biomedical optics*, vol. 22, no. 7, p. 077002, 2017.

[41] N. Bandari, J. Dargahi, and M. Packirisamy, "Miniaturized optical force sensor for minimally invasive surgery with learning-based nonlinear calibration," *IEEE Sensors Journal*, vol. 20, no. 7, pp. 3579–3592, 2020.

[42] J. Dargahi, S. Sokhanvar, S. Najarian, and S. Arbatani, *Tactile sensing and displays: haptic feedback for minimally invasive surgery and robotics*. John Wiley & Sons, 2012.

[43] A. Degani, H. Choset, A. Wolf, and M. A. Zenati, "Highly articulated robotic probe for minimally invasive surgery," in *Proceedings 2006 IEEE International Conference on Robotics and Automation, 2006. ICRA 2006*. IEEE, 2006, pp. 4167–4172.

[44] H. B. Gilbert, J. Neimat, and R. J. Webster, "Concentric tube robots as steerable needles: Achieving follow-the-leader deployment," *IEEE Transactions on Robotics*, vol. 31, no. 2, pp. 246–258, 2015.

[45] Y.-J. Kim, S. Cheng, S. Kim, and K. Iagnemma, "A novel layer jamming mechanism with tunable stiffness capability for minimally invasive surgery," *IEEE Transactions on Robotics*, vol. 29, no. 4, pp. 1031–1042, 2013.

[46] S. B. Kesner and R. D. Howe, "Robotic catheter cardiac ablation combining ultrasound guidance and force control," *The International Journal of Robotics Research*, vol. 33, no. 4, pp. 631–644, 2014.

[47] S. Norouzi-Ghazbi and F. Janabi-Sharifi, "Dynamic modeling and system identification of internally actuated, small-sized continuum robots," *Mechanism and Machine Theory*, vol. 154, p. 104043, 2020.

[48] J. M. Tobis and I. Abudayyeh, "New devices and technology in interventional cardiology," *Journal of cardiology*, vol. 65, no. 1, pp. 5–16, 2015.

[49] S. Hascoet, A. Fraisse, and M. Elbaz, "Successful percutaneous transcatheter patent foramen ovale closure through the right internal jugular vein using a steerable catheter," *Catheterization and cardiovascular interventions*, vol. 82, no. 4, pp. E598–E602, 2013.

[50] J. Joseph, K. CK Wong, M. R Ginks, Y. Bashir, T. R Betts, and K. Rajappan, "Steerable sheath technology in the ablation of atrial fibrillation," *Recent Patents on Cardiovascular Drug Discovery (Discontinued)*, vol. 8, no. 3, pp. 171–177, 2013.

[51] R. C. Diggery and D. T. Grint, *Catheters: Types, Applications, and Potential Complications*. Nova Science, 2012.

[52] "Bleeding or hematoma after cardiac catheterization," 2020, accessed = 2020. [Online]. Available: https://www.fairview.org/Patient-Education/Articles/English/b/l/e/e/d/Bleeding_or_Hematoma_After_Cardiac_Catheterization_116801en

[53] A. Ali, D. H. Plettenburg, and P. Breedveld, "Steerable catheters in cardiology: Classifying steerability and assessing future challenges," *IEEE Transactions on Biomedical Engineering*, vol. 63, no. 4, pp. 679–693, 2016.

[54] C. Piorkowski, C. Eitel, S. Rolf, K. Bode, P. Sommer, T. Gaspar, S. Kircher, U. Wetzel, A. S. Parwani, L.-H. Boldt *et al.*, "Steerable versus nonsteerable sheath technology in atrial fibrillation ablation: a prospective, randomized study," *Circulation: Arrhythmia and Electrophysiology*, vol. 4, no. 2, pp. 157–165, 2011.

[55] A. Arya, G. Hindricks, P. Sommer, Y. Huo, A. Bollmann, T. Gaspar, K. Bode, D. Husser, H. Kottkamp, and C. Piorkowski, "Long-term results and the predictors of outcome of catheter ablation of atrial fibrillation using steerable sheath catheter navigation after single procedure in 674 patients," *Europace*, vol. 12, no. 2, pp. 173–180, 2010.

[56] W. Ullah, R. J. Hunter, A. McLean, M. Dhinoja, M. J. Earley, S. Sporton, and R. J. Schilling, "Impact of steerable sheaths on contact forces and reconnection sites in ablation for persistent atrial fibrillation," *Journal of cardiovascular electrophysiology*, vol. 26, no. 3, pp. 266–273, 2015.

[57] T. Kimura, S. Takatsuki, A. Oishi, M. Negishi, S. Kashimura, Y. Katsumata, T. Nishiyama, N. Nishiyama, Y. Tanimoto, Y. Aizawa *et al.*, "Operator-blinded contact force monitoring during pulmonary vein isolation using conventional and steerable sheaths," *International journal of cardiology*, vol. 177, no. 3, pp. 970–976, 2014.

[58] D. B. Camarillo, C. R. Carlson, and J. K. Salisbury, "Configuration tracking for continuum manipulators with coupled tendon drive," *IEEE transactions on robotics*, vol. 25, no. 4, pp. 798–808, 2009.

[59] R. Ozawa, H. Kobayashi, and K. Hashirii, "Analysis, classification, and design of tendon-driven mechanisms," *IEEE transactions on robotics*, vol. 30, no. 2, pp. 396–410, 2013.

[60] J. S. Mehling, M. A. Diftler, M. Chu, and M. Valvo, "A minimally invasive tendril robot for in-space inspection," in *The First IEEE/RAS-EMBS International Conference on Biomedical Robotics and Biomechatronics, 2006. BioRob 2006.* IEEE, 2006, pp. 690–695.

[61] R. A. Beasley, "Medical robots: current systems and research directions," *Journal of Robotics*, vol. 2012, 2012.

[62] Y. Ganji, F. Janabi-Sharifi *et al.*, "Catheter kinematics for intracardiac navigation," *IEEE Transactions on Biomedical Engineering*, vol. 56, no. 3, pp. 621–632, 2009.

[63] D. B. Camarillo, C. F. Milne, C. R. Carlson, M. R. Zinn, and J. K. Salisbury, "Mechanics modeling of tendon-driven continuum manipulators," *IEEE transactions on robotics*, vol. 24, no. 6, pp. 1262–1273, 2008.

[64] I. D. Walker, "Continuous backbone "continuum" robot manipulators," *International Scholarly Research Notices*, vol. 2013, 2013.

[65] "Catheter positioning surgical robot sensei ® x." [Online]. Available: https://www.medicalexpo.com/prod/hansen-medical/product-99069-639797.html

[66] S. Hirose, "Biologically inspired robots," *Snake-Like Locomotors and Manipulators*, 1993.

[67] I. A. Gravagne, C. D. Rahn, and I. D. Walker, "Large deflection dynamics and control for planar continuum robots," *IEEE/ASME transactions on mechatronics*, vol. 8, no. 2, pp. 299–307, 2003.

[68] J.-B. Le Polain De Waroux, R. Weerasooriya, K. Anvardeen, C. Barbraud, S. Marchandise, C. De Meester, C. Goesaert, I. Reis, and C. Scavee, "Low contact force and force–time integral predict early recovery and dormant conduction revealed by adenosine after pulmonary vein isolation," *Ep Europace*, vol. 17, no. 6, pp. 877–883, 2015.

[69] B. Bardou, P. Zanne, F. Nageotte, and M. de Mathelin, "Control of a multiple sections flexible endoscopic system," in *2010 IEEE/RSJ International Conference on Intelligent Robots and Systems*. IEEE, 2010, pp. 2345–2350.

[70] Q. Zhao and F. Gao, "Design and analysis of a kind of biomimetic continuum robot," in *2010 IEEE International Conference on Robotics and Biomimetics*. IEEE, 2010, pp. 1316–1320.

[71] A. Jiang, G. Xynogalas, P. Dasgupta, K. Althoefer, and T. Nanayakkara, "Design of a variable stiffness flexible manipulator with composite granular jamming and membrane coupling," in *2012 IEEE/RSJ International Conference on Intelligent Robots and Systems*. IEEE, 2012, pp. 2922–2927.

[72] M. Giorelli, F. Renda, M. Calisti, A. Arienti, G. Ferri, and C. Laschi, "A two dimensional inverse kinetics model of a cable driven manipulator inspired by the octopus arm," in *2012 IEEE international conference on robotics and automation*. IEEE, 2012, pp. 3819–3824.

[73] J. Shang, C. J. Payne, J. Clark, D. P. Noonan, K.-W. Kwok, A. Darzi, and G.-Z. Yang, "Design of a multitasking robotic platform with flexible arms and articulated head for minimally invasive surgery," in *2012 IEEE/RSJ International Conference on Intelligent Robots and Systems*. IEEE, 2012, pp. 1988–1993.

[74] M. W. Hannan and I. D. Walker, "Kinematics and the implementation of an elephant's trunk manipulator and other continuum style robots," *Journal of robotic systems*, vol. 20, no. 2, pp. 45–63, 2003.

[75] H.-S. Yoon, S. M. Oh, J. H. Jeong, S. H. Lee, K. Tae, K.-C. Koh, and B.-J. Yi, "Active bending endoscope robot system for navigation through sinus area," in *2011 IEEE/RSJ International Conference on Intelligent Robots and Systems*. IEEE, 2011, pp. 967–972.

[76] H. Watanabe, K. Kanou, Y. Kobayashi, and M. G. Fujie, "Development of a" steerable drill" for acl reconstruction to create the arbitrary trajectory of a bone tunnel," in *2011 IEEE/RSJ International Conference on Intelligent Robots and Systems*. IEEE, 2011, pp. 955–960.

[77] N. Simaan, R. Taylor, and P. Flint, "A dexterous system for laryngeal surgery," in *IEEE International Conference on Robotics and Automation, 2004. Proceedings. ICRA'04. 2004*, vol. 1. IEEE, 2004, pp. 351–357.

[78] T. N. Do., T. Tjahjowidodo., M. W. S. Lau., and S. J. Phee., "Adaptive control of position compensation for cable-conduit mechanisms used in flexible surgical robots," in *Proceedings of the 11th International Conference on Informatics in Control, Automation and Robotics - Volume 2: ICINCO,*, INSTICC. SciTePress, 2014, pp. 110–117.

[79] H. M. Le, T. N. Do, and S. J. Phee, "A survey on actuators-driven surgical robots," *Sensors and Actuators A: Physical*, vol. 247, pp. 323–354, 2016.

[80] Y. Fu, H. Liu, W. Huang, S. Wang, and Z. Liang, "Steerable catheters in minimally invasive vascular surgery," *The International Journal of Medical Robotics and Computer Assisted Surgery*, vol. 5, no. 4, pp. 381–391, 2009.

[81] R. Deimel and O. Brock, "A novel type of compliant and underactuated robotic hand for dexterous grasping," *The International Journal of Robotics Research*, vol. 35, no. 1-3, pp. 161–185, 2016.

[82] ——, "A compliant hand based on a novel pneumatic actuator," in *2013 IEEE International Conference on Robotics and Automation*. IEEE, 2013, pp. 2047–2053.

[83] R. R. Miles, D. L. Schumann, M. A. Pearson, and D. Hilken, "Steerable catheter with distending lumen-actuated curling catheter tip," Jan. 14 2010, uS Patent App. 12/502,097.

[84] T. Gagarina and P. Joli, "Modeling and experimental analysis of a new bellow type actuators for active catheter end-effector," in *Proceedings 10th IEEE International Workshop on Robot and Human Interactive Communication. ROMAN 2001 (Cat. No. 01TH8591)*. IEEE, 2001, pp. 612–617.

[85] Y. Haga, Y. Muyari, T. Mineta, T. Matsunaga, H. Akahori, and M. Esashi, "Small diameter hydraulic active bending catheter using laser processed super elastic alloy and silicone rubber tube," in *2005 3rd IEEE/EMBS Special Topic Conference on Microtechnology in Medicine and Biology*. IEEE, 2005, pp. 245–248.

[86] M. Ikeuchi and K. Ikuta, ""membrane micro emboss following excimer laser ablation (meme-x) process" for pressure-driven micro active catheter," in *2008 IEEE 21st International Conference on Micro Electro Mechanical Systems*. IEEE, 2008, pp. 62–65.

[87] H. Lipson, "Challenges and opportunities for design, simulation, and fabrication of soft robots," *Soft Robotics*, vol. 1, no. 1, pp. 21–27, 2014.

[88] Y. Elsayed, A. Vincensi, C. Lekakou, T. Geng, C. Saaj, T. Ranzani, M. Cianchetti, and A. Menciassi, "Finite element analysis and design optimization of a pneumatically actuating silicone module for robotic surgery applications," *Soft Robotics*, vol. 1, no. 4, pp. 255–262, 2014.

[89] M. Luo, M. Agheli, and C. D. Onal, "Theoretical modeling and experimental analysis of a pressure-operated soft robotic snake," *Soft Robotics*, vol. 1, no. 2, pp. 136–146, 2014.

[90] Y. Sun, Y. S. Song, and J. Paik, "Characterization of silicone rubber based soft pneumatic actuators," in *2013 IEEE/RSJ International Conference on Intelligent Robots and Systems*. Ieee, 2013, pp. 4446–4453.

[91] P. Polygerinos, Z. Wang, J. T. Overvelde, K. C. Galloway, R. J. Wood, K. Bertoldi, and C. J. Walsh, "Modeling of soft fiber-reinforced bending actuators," *IEEE Transactions on Robotics*, vol. 31, no. 3, pp. 778–789, 2015.

[92] F. Ilievski, A. D. Mazzeo, R. F. Shepherd, X. Chen, and G. M. Whitesides, "Soft robotics for chemists," *Angewandte Chemie*, vol. 123, no. 8, pp. 1930–1935, 2011.

[93] R. V. Martinez, J. L. Branch, C. R. Fish, L. Jin, R. F. Shepherd, R. M. Nunes, Z. Suo, and G. M. Whitesides, "Robotic tentacles with three-dimensional mobility based on flexible elastomers," *Advanced materials*, vol. 25, no. 2, pp. 205–212, 2013.

[94] B. L. Nguyen, J. L. Merino, and E. S. Gang, "Remote navigation for ablation procedures–a new step forward in the treatment of cardiac arrhythmias," *European Cardiology*, vol. 6, no. 3, pp. 50–56, 2010.

[95] M. N. Faddis, W. Blume, J. Finney, A. Hall, J. Rauch, J. Sell, K. T. Bae, M. Talcott, and B. Lindsay, "Novel, magnetically guided catheter for endocardial mapping and radiofrequency catheter ablation," *Circulation*, vol. 106, no. 23, pp. 2980–2985, 2002.

[96] A. Govari, A. C. Altmann, Y. Ephrath, and C. T. Beeckler, "Robotic drive for catheter," Apr. 14 2015, uS Patent 9,005,217.

[97] S. R. Atmakuri, E. I. Lev, C. Alviar, E. Ibarra, A. E. Raizner, S. L. Solomon, and N. S. Kleiman, "Initial experience with a magnetic navigation system for percutaneous coronary intervention in complex coronary artery lesions," *Journal of the American College of Cardiology*, vol. 47, no. 3, pp. 515–521, 2006.

[98] C. Pappone, G. Vicedomini, F. Manguso, F. Gugliotta, P. Mazzone, S. Gulletta, N. Sora, S. Sala, A. Marzi, G. Augello *et al.*, "Robotic magnetic navigation for atrial fibrillation ablation," *Journal of the American College of Cardiology*, vol. 47, no. 7, pp. 1390–1400, 2006.

[99] M. Cianchetti, C. Laschi, A. Menciassi, and P. Dario, "Biomedical applications of soft robotics," *Nature Reviews Materials*, vol. 3, no. 6, pp. 143–153, 2018.

[100] E. Ayvali, C.-P. Liang, M. Ho, Y. Chen, and J. P. Desai, "Towards a discretely actuated steerable cannula for diagnostic and therapeutic procedures," *The International journal of robotics research*, vol. 31, no. 5, pp. 588–603, 2012.

[101] M. Langelaar and F. van Keulen, "Modeling of a shape memory alloy active catheter," in *45th AIAA/ASME/ASCE/AHS/ASC Structures, Structural Dynamics & Materials Conference*, 2004, p. 1653.

[102] L. Zhang, S. Guo, H. Yu, and Y. Song, "Performance evaluation of a strain-gauge force sensor for a haptic robot-assisted catheter operating system," *Microsystem Technologies*, vol. 23, no. 10, pp. 5041–5050, 2017.

[103] Y. Fu, A. Gao, H. Liu, and S. Guo, "The master-slave catheterisation system for positioning the steerable catheter," *International Journal of Mechatronics and Automation*, vol. 1, no. 3-4, pp. 143–152, 2011.

[104] N. Bandari, J. Dargahi, and M. Packirisamy, "Optical fiber array sensor for force estimation and localization in tavi procedure: Design, modeling, analysis and validation," *Sensors*, vol. 21, no. 16, p. 5377, 2021.

[105] S. Guo, M. Qin, N. Xiao, Y. Wang, W. Peng, and X. Bao, "High precise haptic device for the robotic catheter navigation system," in *2016 IEEE International Conference on Mechatronics and Automation*. IEEE, 2016, pp. 2524–2529.

[106] S. Chao, T. Ren, S. Gales, and M. Holl, "Ieee/ras-embs international conference on biomedical robotics and biomechatronics," 2006.

[107] S. Hasanzadeh and F. Janabi-Sharifi, "Model-based force estimation for intracardiac catheters," *IEEE/ASME Transactions on Mechatronics*, vol. 21, no. 1, pp. 154–162, 2015.

[108] M. Jolaei, "Design, development and force control of a tendon-driven steerable catheter with a learning-based approach," Ph.D. dissertation, Concordia University, 2020.

[109] Y. Bailly and Y. Amirat, "Modeling and control of a hybrid continuum active catheter for aortic aneurysm treatment," in *Proceedings of the 2005 IEEE International Conference on Robotics and Automation*. IEEE, 2005, pp. 924–929.

[110] R. J. Webster III and B. A. Jones, "Design and kinematic modeling of constant curvature continuum robots: A review," *The International Journal of Robotics Research*, vol. 29, no. 13, pp. 1661–1683, 2010.

[111] M. Khoshnam, M. Azizian, and R. V. Patel, "Modeling of a steerable catheter based on beam theory," in *2012 IEEE International Conference on Robotics and Automation*. IEEE, 2012, pp. 4681–4686.

[112] M. Khoshnam and R. V. Patel, "Estimating contact force for steerable ablation catheters based on shape analysis," in *2014 IEEE/RSJ International Conference on Intelligent Robots and Systems*. IEEE, 2014, pp. 3509–3514.

[113] M. Khoshnam, A. C. Skanes, and R. V. Patel, "Modeling and estimation of tip contact force for steerable ablation catheters," *IEEE Transactions on Biomedical Engineering*, vol. 62, no. 5, pp. 1404–1415, 2015.

[114] B. Gao, S. Guo, N. Xiao, and J. Guo, "Design of the virtual reality based robotic catheter system for minimally invasive surgery training," in *2012 IEEE International Conference on Automation and Logistics*. IEEE, 2012, pp. 611–616.

[115] B. A. Jones and I. D. Walker, "Kinematics for multisection continuum robots," *IEEE Transactions on Robotics*, vol. 22, no. 1, pp. 43–55, 2006.

[116] A. A. Shabana, "Flexible multibody dynamics: review of past and recent developments," *Multibody system dynamics*, vol. 1, no. 2, pp. 189–222, 1997.

[117] T. Alderliesten, M. K. Konings, and W. J. Niessen, "Simulation of minimally invasive vascular interventions for training purposes," *Computer Aided Surgery*, vol. 9, no. 1-2, pp. 3–15, 2004.

[118] P. Flores and H. M. Lankarani, *Contact force models for multibody dynamics*. Springer, 2016, vol. 226.

[119] M. Camara, E. Mayer, A. Darzi, and P. Pratt, "Soft tissue deformation for surgical simulation: a position-based dynamics approach," *International journal of computer assisted radiology and surgery*, vol. 11, no. 6, pp. 919–928, 2016.

[120] S. Li, Q. Xia, A. Hao, H. Qin, and Q. Zhao, "Haptics-equiped interactive pci simulation for patient-specific surgery training and rehearsing," *Science China Information Sciences*, vol. 59, no. 10, pp. 1–6, 2016.

[121] J. Lenoir, S. Cotin, C. Duriez, and P. Neumann, "Interactive physically-based simulation of catheter and guidewire," *Computers & Graphics*, vol. 30, no. 3, pp. 416–422, 2006.

[122] F. Jourdan, P. Alart, and M. Jean, "A gauss-seidel like algorithm to solve frictional contact problems," *Computer methods in applied mechanics and engineering*, vol. 155, no. 1-2, pp. 31–47, 1998.

[123] M. Konings, E. Van de Kraats, T. Alderliesten, and W. Niessen, "Analytical guide wire motion algorithm for simulation of endovascular interventions," *Medical and Biological Engineering and Computing*, vol. 41, no. 6, pp. 689–700, 2003.

[124] P. P. Valentini and E. Pennestrì, "Modeling elastic beams using dynamic splines," *Multibody system dynamics*, vol. 25, no. 3, pp. 271–284, 2011.

[125] F. M. Cardoso and S. S. Furuie, "Guidewire path determination for intravascular applications," *Computer methods in biomechanics and biomedical engineering*, vol. 19, no. 6, pp. 628–638, 2016.

[126] A. Hooshiar, A. Sayadi, M. Jolaei, and J. Dargahi, "Accurate estimation of tip force on tendon-driven catheters using inverse cosserat rod model," in *2020 International Conference on Biomedical Innovations and Applications (BIA)*. IEEE, 2020, pp. 37–40.

[127] G. S. Chirikjian, "Hyper-redundant manipulator dynamics: A continuum approximation," *Advanced Robotics*, vol. 9, no. 3, pp. 217–243, 1994.

[128] K.-J. Bathe and S. Bolourchi, "Large displacement analysis of three-dimensional beam structures," *International journal for numerical methods in engineering*, vol. 14, no. 7, pp. 961–986, 1979.

[129] G. Robinson and J. B. C. Davies, "Continuum robots-a state of the art," in *Proceedings 1999 IEEE international conference on robotics and automation (Cat. No. 99CH36288C)*, vol. 4. IEEE, 1999, pp. 2849–2854.

[130] D. C. Rucker and R. J. Webster, "Mechanics of bending, torsion, and variable precurvature in multi-tube active cannulas," in *2009 IEEE International Conference on Robotics and Automation*. IEEE, 2009, pp. 2533–2537.

[131] D. C. Rucker, R. J. Webster III, G. S. Chirikjian, and N. J. Cowan, "Equilibrium conformations of concentric-tube continuum robots," *The International journal of robotics research*, vol. 29, no. 10, pp. 1263–1280, 2010.

[132] A. Degirmenci, P. M. Loschak, C. M. Tschabrunn, E. Anter, and R. D. Howe, "Compensation for unconstrained catheter shaft motion in cardiac catheters," in *2016 IEEE International Conference on Robotics and Automation (ICRA)*. IEEE, 2016, pp. 4436–4442.

[133] P. Yaftian, N. Bandari, A. Hooshiar, and J. Dargahi, "Image-based contact detection and static force estimation on steerable rfa catheters," in *2020 International Conference on Biomedical Innovations and Applications (BIA)*. IEEE, 2020, pp. 57–60.

[134] P. Yaftian, N. Bandari, and J. Dargahi, "Comparison of mechanistic and learning-based tip force estimation on tendon-driven soft robotic catheters," in *2022 ACM/IEEE International Conference on Human-Robot Interaction (HRI), (Under review)*. IEEE, 2022.

[135] ——, "Comparison of mechanistic and learning-based tip force estimation on tendon-driven soft robotic catheters," in *IEEE transactions on instrumentation and measuremen, (Under review).*, 2021.

[136] K. G. Graves, V. Jacobs, H. T. May, M. J. Cutler, J. D. Day, and T. J. Bunch, "Atrial fibrillation ablation and its impact on stroke," *Current treatment options in cardiovascular medicine*, vol. 20, no. 1, p. 2, 2018.

[137] M. Jolaei, A. Hooshiar, J. Dargahi, and M. Packirisamy, "Toward task autonomy in robotic cardiac ablation: Learning-based kinematic control of soft tendon-driven catheters," *Soft Robotics*, vol. Accepted, 2020.

[138] S. Guo, Y. Song, X. Yin, L. Zhang, T. Tamiya, H. Hirata, and H. Ishihara, "A novel robot-assisted endovascular catheterization system with haptic force feedback," *IEEE Transactions on Robotics*, vol. 35, no. 3, pp. 685–696, 2019.

[139] L. Zou, C. Ge, Z. J. Wang, E. Cretu, and X. Li, "Novel tactile sensor technology and smart tactile sensing systems: A review," *Sensors*, vol. 17, no. 11, p. 2653, 2017.

[140] M. Luo, H. Xie, L. Xie, P. Cai, and L. Gu, "A robust and real-time vascular intervention simulation based on kirchhoff elastic rod," *Computerized medical imaging and graphics*, vol. 38, no. 8, pp. 735–743, 2014.

[141] M. Jolaei, A. Hooshiar, A. Sayadi, J. Dargahi, and M. Packirisamy, "Sensor-free force control of tendon-driven ablation catheters through position control and contact modeling," in *2019 41st Annual International Conference of the IEEE Engineering in Medicine and Biology Society (EMBC)*. IEEE, 2020(In-Press), pp. 1–4.

[142] P. Lanzer, *Catheter-based cardiovascular interventions: A knowledge-based approach*. Springer Science & Business Media, 2012.

[143] D. Mozaffarian, E. J. Benjamin, A. S. Go, D. K. Arnett, M. J. Blaha, M. Cushman, S. De Ferranti, J.-P. Després, H. J. Fullerton, V. J. Howard *et al.*, "Executive summary: heart disease and stroke statistics—2015 update: a report from the american heart association," *Circulation*, vol. 131, no. 4, pp. 434–441, 2015.

[144] M. Jolaei, A. Hooshiar, J. Dargahi, and M. Packirisamy, "Toward task autonomy in robotic cardiac ablation: Learning-based kinematic control of soft tendon-driven catheters," *Soft Robotics*, 2020.

[145] R. Amuthan and A. B. Curtis, "What clinical trials of ablation for atrial fibrillation tell us–and what they do not," *Heart Rhythm O2*, 2021.

[146] A. Natale, V. Y. Reddy, G. Monir, D. J. Wilber, B. D. Lindsay, H. T. McElderry, C. Kantipudi, M. C. Mansour, D. P. Melby, D. L. Packer *et al.*, "Paroxysmal af catheter ablation with a contact force sensing catheter: results of the prospective, multicenter smart-af trial," *Journal of the American College of Cardiology*, vol. 64, no. 7, pp. 647–656, 2014.

[147] V. Y. Reddy, S. R. Dukkipati, P. Neuzil, A. Natale, J.-P. Albenque, J. Kautzner, D. Shah, G. Michaud, M. Wharton, D. Harari *et al.*, "Randomized, controlled trial of the safety and effectiveness of a contact force–sensing irrigated catheter for ablation of paroxysmal atrial fibrillation: results of the tacticath contact force ablation catheter study for atrial fibrillation (toccastar) study," *Circulation*, vol. 132, no. 10, pp. 907–915, 2015.

[148] P. Aagaard, A. Natale, and L. Di Biase, "Robotic navigation for catheter ablation: benefits and challenges," *Expert review of medical devices*, vol. 12, no. 4, pp. 457–469, 2015.

[149] F. Jelínek, E. A. Arkenbout, P. W. Henselmans, R. Pessers, and P. Breedveld, "Classification of joints used in steerable instruments for minimally invasive surgery—a review of the state of the art," *Journal of Medical Devices*, vol. 9, no. 1, 2015.

[150] J. Till, V. Aloi, and C. Rucker, "Real-time dynamics of soft and continuum robots based on cosserat rod models," *The International Journal of Robotics Research*, vol. 38, no. 6, pp. 723–746, 2019.

[151] J. Guo, S. Guo, N. Xiao, and B. Gao, "Virtual reality simulators based on a novel robotic catheter operating system for training in minimally invasive surgery," *Journal of Robotics and Mechatronics*, vol. 24, no. 4, p. 649, 2012.

[152] S. Cotin, C. Duriez, J. Lenoir, P. Neumann, and S. Dawson, "New approaches to catheter navigation for interventional radiology simulation," in *International Conference on Medical Image Computing and Computer-Assisted Intervention*. Springer, 2005, pp. 534–542.

[153] C. Della Santina, R. L. Truby, and D. Rus, "Data–driven disturbance observers for estimating external forces on soft robots," *IEEE Robotics and Automation Letters*, vol. 5, no. 4, pp. 5717–5724, 2020.

[154] R. Yasin and N. Simaan, "Joint-level force sensing for indirect hybrid force/position control of continuum robots with friction," *The International Journal of Robotics Research*, p. 0278364920979721, 2020.

[155] F. Qi, F. Ju, D. Bai, Y. Wang, and B. Chen, "Kinematic analysis and navigation method of a cable-driven continuum robot used for minimally invasive surgery," *The International Journal of Medical Robotics and Computer Assisted Surgery*, vol. 15, no. 4, p. e2007, 2019.

[156] X.-R. Cheng, Q.-K. Song, X.-L. Xie, L. Cheng, L. Wang, G.-B. Bian, Z.-G. Hou, T. Huang, and P. Prasong, "A fast and stable guidewire model for minimally invasive vascular surgery

based on lagrange multipliers," in *2017 Seventh International Conference on Information Science and Technology (ICIST)*. IEEE, 2017, pp. 109–114.

[157] M. Jolaei, A. Hooshiar, A. Sayadi, J. Dargahi, and M. Packirisamy, "Sensor-free force control of tendon-driven ablation catheters through position control and contact modeling," in *2020 42nd Annual International Conference of the IEEE Engineering in Medicine & Biology Society (EMBC)*. IEEE, 2020, pp. 5248–5251.

[158] H. Donat, S. Lilge, J. Burgner-Kahrs, and J. J. Steil, "Estimating tip contact forces for concentric tube continuum robots based on backbone deflection," *IEEE Transactions on Medical Robotics and Bionics*, vol. 2, no. 4, pp. 619–630, 2020.

[159] A. J. Sanfilippo, V. M. Abascal, M. Sheehan, L. B. Oertel, P. Harrigan, R. A. Hughes, and A. E. Weyman, "Atrial enlargement as a consequence of atrial fibrillation. a prospective echocardiographic study." *Circulation*, vol. 82, no. 3, pp. 792–797, 1990.

[160] M. Govindan, A. Kiotsekoglou, S. K. Saha, and A. J. Camm, "Right atrial myocardial deformation by two-dimensional speckle tracking echocardiography predicts recurrence in paroxysmal atrial fibrillation," *Journal of echocardiography*, vol. 15, no. 4, pp. 166–175, 2017.

[161] M. Hannan and I. Walker, "Vision based shape estimation for continuum robots," in *2003 IEEE International Conference on Robotics and Automation (Cat. No. 03CH37422)*, vol. 3. IEEE, 2003, pp. 3449–3454.

[162] A. Wahrburg, J. Bös, K. D. Listmann, F. Dai, B. Matthias, and H. Ding, "Motor-current-based estimation of cartesian contact forces and torques for robotic manipulators and its application to force control," *IEEE Transactions on Automation Science and Engineering*, vol. 15, no. 2, pp. 879–886, 2017.

[163] B. Zhao and C. A. Nelson, "Sensorless force sensing for minimally invasive surgery," *Journal of medical devices*, vol. 9, no. 4, 2015.

[164] F. Squara, D. G. Latcu, Y. Massaad, M. Mahjoub, S.-S. Bun, and N. Saoudi, "Contact force and force-time integral in atrial radiofrequency ablation predict transmurality of lesions," *Europace*, vol. 16, no. 5, pp. 660–667, 2014.

[165] N. Bandari, J. Dargahi, and M. Packirisamy, "Image-based optical-fiber force sensor for minimally invasive surgery with ex-vivo validation," *Journal of The Electrochemical Society*, vol. 167, no. 12, p. 127504, 2020.

[166] S. Hasanzadeh and F. Janabi-Sharifi, "Model-based force estimation for intracardiac catheters," *IEEE/ASME Transactions on Mechatronics*, vol. 21, pp. 154–162, 2016.

[167] H. Rafii-Tari, J. Liu, S.-L. Lee, C. Bicknell, and G.-Z. Yang, "Learning-based modeling of endovascular navigation for collaborative robotic catheterization," in *International conference on medical image computing and computer-assisted intervention*. Springer, 2013, pp. 369–377.

[168] W. Chi, J. Liu, H. Rafii-Tari, C. Riga, C. Bicknell, and G.-Z. Yang, "Learning-based endovascular navigation through the use of non-rigid registration for collaborative robotic catheterization," *International journal of computer assisted radiology and surgery*, vol. 13, no. 6, pp. 855–864, 2018.

[169] D. Braganza, D. Dawson, I. D. Walker, and N. Nath, "Neural network grasping controller for continuum robots," in *Proceedings of the 45th IEEE Conference on Decision and Control*. IEEE, 2006, pp. 6445–6449.

[170] S. Abeywardena, Q. Yuan, A. Tzemanaki, E. Psomopoulou, L. Droukas, C. Melhuish, and S. Dogramadzi, "Estimation of tool-tissue forces in robot-assisted minimally invasive surgery using neural networks," *Frontiers in Robotics and AI*, vol. 6, p. 56, 2019.

[171] N. Tran, J. Y. Wu, A. Deguet, and P. Kazanzides, "A deep learning approach to intrinsic force sensing on the da vinci surgical robot," in *2020 Fourth IEEE International Conference on Robotic Computing (IRC)*. IEEE, 2020, pp. 25–32.

[172] A. Géron, *Hands-on machine learning with Scikit-Learn, Keras, and TensorFlow: Concepts, tools, and techniques to build intelligent systems*. O'Reilly Media, 2019.